
The FY-3D Global Active Fire product: Principle, Methodology and Validation

Jie Chen^{1,2} †, Qi Yao³ †, Ziyue Chen^{3*}, Manchun Li⁴, Zhaozhan Hao⁵, Cheng Liu^{1,2}, Wei Zheng^{1,2}, Miaoqing Xu³, Xiao Chen³, Jing Yang³, Qiancheng Lv³, Bingbo Gao^{5*}

¹ Innovation Center for FengYun Meteorological Satellite, National Satellite Meteorological Center (National Center for Space Weather), China Meteorological Administration, Beijing 100081, China

² Key Laboratory of Radiometric Calibration and Validation for Environmental Satellites, National Satellite Meteorological Center (National Center for Space Weather), China Meteorological Administration, Beijing 100081, China³ College of Global Change and Earth System Science, Beijing Normal University, Beijing 100091, China

⁴ School of Geography and Ocean Sciences, Nanjing University, Nanjing 210008, China

⁵ College of Land Science and Technology, China Agricultural University, Beijing 100083, China

†These authors contributed equally.

*Correspondence to: Ziyue Chen (zychen@bnu.edu.cn) or Bingbo Gao (gaobingbo@cau.edu.cn)

Abstract. Wild fires have a strong negative effect on environment, ecology and public health. However, the potential degradation of mainstream global fire products leads to large uncertainty on the effective monitoring of wild fires and its influence. To fill this gap, we produced FY-3D global fire products with a similar spatial and temporal resolution, aiming to serve as the alternative and continuity for MODIS global fire products. Firstly, the sensor parameters and major algorithms for noise detection and fire identification in FY-3D products were introduced. For visual-check-based accuracy assessment, five typical regions, Africa, South America, Indo-China Peninsula, Siberia and Australia, across the globe were selected and the overall accuracy exceeded 94%. Meanwhile, the consistence between FY-3D and MODIS fire products was examined. The result suggested that the overall consistence was 84.4%, with a fluctuation across seasons, surface types and regions. The high accuracy and consistence with MODIS products proved that FY-3D fire product was an ideal tool for global fire monitoring. Based on field-collected reference data, we further evaluated the suitability of FY-3D fire products in China. The overall accuracy and accuracy (without considering omission errors) was 79.43% and 88.50% respectively, higher than that of MODIS fire products. Since detailed local geographical conditions were specifically considered, FY-3D products should be preferably employed for fires monitoring in China. FY-3D fire dataset can be downloaded at <http://satellite.nsmc.org.cn/portalsite/default.aspx> (NSMC, 2021).

1 Introduction

More than half of global land surfaces have been influenced by wild fires and the total global burned area summed up to the area of European Union every year (Andela et al., 2019; Keeley et al., 2011; Moritz et al., 2012). Wild fires, especially large-scale wild fires, in forests, grasslands and farmlands have a significant impact on crop productivity (Jethva et al., 2019), atmospheric pollution (Guo et al., 2020), biodiversity (Kelly et al., 2020), climate change (Alisjahbana et al., 2017; Keegan et al., 2014) and public health (Huff et al., 2015; Johnston et al., 2012; Oliveira et al., 2020; Yuchi et al., 2016). In recent years,

38 the increasing events of forest fires in China, US, Australia, and Amazon Rain Forests and grassland fires
39 in Mongolia have caused a large number of casualty (Cochrane, 2003), the lost of millions of wildlife
40 (Wintle et al., 2020), remarkably deteriorated air quality (Guo et al., 2010; Liu et al., 2018; Marlier et al.,
41 2012; Volkova et al., 2019), severely damaged ecosystems (Cerdeira et al., 2012), massive economic losses
42 (Stephenson et al., 2013) and regional or global climate change (Abram et al., 2021; Jacobson, 2014;
43 Twohy et al., 2021; Wang et al., 2020).

44
45 Due to its great influences, growing emphasis has been placed on the monitoring of wild fires based on
46 remote sensing products. Since 1970s, the implementation and research of satellite-based fire detection
47 has started in US using National Oceanic and Atmospheric Administration (NOAA) series satellites
48 (www.noaa.gov, Dozier et al., 1981; Flannigan and Haar et al., 1986; Kaufman et al., 1990; Boles et al.,
49 2000). NOAA fire products, with a spatial resolution of 1.1 km and a daily temporal resolution, have
50 been employed globally for decades, and provide the data support for long time series analysis. In
51 addition to NOAA fire products, a diversity of regional or global fire products has been proposed in
52 recent years.

53
54 Thanks to its easy access, long time series, and reliable accuracy (Giglio et al., 2018), the Moderate
55 Resolution Imaging Spectroradiometer (MODIS) fire product, with a spatial resolution of 1km and a
56 temporal resolution of 12 hours, have been available since 2000 and become one of the most widely
57 employed fire products to monitor the temporal evolution of large-scale wide fires, including forest fires
58 (Mohajane et al., 2021), grassland fires (Zhang et al., 2017) and crop residue burning (Li et al., 2016).
59 With a similar temporal resolution (12 hours), the Visible Infrared Imaging Radiometer Suite (VIIRS)
60 fire products with a spatial resolution of 375m has been available for fire detection since 2011. Despite
61 a higher spatial resolution, VIIRS fire products are produced using less bands than MODIS fire products,
62 and the mainly used 4- μm I-band may lead to large bias in the estimation of FRP (Fire Radiative Power)
63 during an intense fire event (Schroeder et al., 2014). Consequently, VIIRS fire products present a
64 relatively poor consistence with MODIS fire products and the accuracy of VIIRS fire products is
65 generally lower than that of MODIS fire products (Sharma et al., 2017). In this case, VIIRS fire products
66 may not serve as a complete replacement of and should be comprehensively employed with MODIS fire
67 products.

68
69 In recent years, with the growing needs for real-time monitoring of a diversity of environmental issues
70 and ecological process, some satellites have been launched to provide remote sensing products with
71 extremely high temporal resolution. GEOS-16 Advanced Baseline Imager (ABI) active fire products,
72 with a temporal resolution of five minutes and a spatial resolution of 2km, have been available since
73 2017 (Hall et al., 2019). GEOS-ABI fire products can effectively monitor middle to large-scale fires and
74 be used for estimating fire emissions. GEOS-ABI fire products may lead to a poor detection accuracy
75 when identifying small-scale fires (Li et al., 2020). GEOS-ABI mainly provides regional fire products in
76 Southeastern Conterminous United States (CONUS). Himawari-8 products, with a spatial resolution of
77 2 km and temporal resolution of 10 minutes, have been widely employed to monitor meteorology and

78 wild fires in Asia and Australia since 2015 (Xu et al. 2017). Similar to GEOS-16 ABI fire products,
79 Himawari-8 fire products are also limited in effectively detecting small-scale fires (Wickramasinghe et
80 al., 2018). Despite an extremely high temporal resolution, fire products produced using geostationary
81 satellites only cover a regional area and cannot monitor the distribution and evolution of wild fires at a
82 global scale.

83

84 Long-term running leads to the aging of sensors (Sayer et al., 2015; Liu et al., 2017; Barnes et al., 2019)
85 and causes the degradation of sensor sensitivities (Lyapustin et al., 2014; Doelling et al., 2015; Xiong et
86 al., 2019), increased system errors (Fensholt et al., 2012; Xie et al., 2011) and decreased product quality
87 (Fang et al., 2012; Wang et al., 2012). With a high temporal resolution and so far the longest time series,
88 MODIS global fire products have become the most important data source for examining historical
89 regional and global fires, monitoring occurring fires, and investigating their environmental influences.
90 However, after twenty-two years' running, the gradual ageing of sensors will, if not already, cause the
91 future degradation of MODIS global fire products. To continuously make full use of the existing long-
92 term series of MODIS fire product, even if it degrades or stops services in the future, a fire product with
93 good reliability, good consistence and similar characteristics is urgently needed to serve as the potential
94 alternative and continuity of global MODIS fire products. Since the launch of Fengyun-3C (FY-3C)
95 satellite in September, 2013, a series of FY meteorological satellites have been designed to produce global
96 active fire products. FY-3C VIRR fire products were produced based on an effective active fire detection
97 algorithm (Lin et al., 2017), which considered dynamic thresholds and infrared gradients. However, the
98 overall accuracy of FY-3C VIRR fire products remained unsatisfactory at the global scale and are thus
99 not publicly released.

100 In November, 2017, Fengyun-3D (FY-3D) satellite was launched with an improved Medium Resolution
101 Spectral Imager (MERSI) for fire detection. With a similar spatiotemporal resolution, FY-3D provides a
102 promising solution for the continuity of global MODIS fire products. In this paper, we introduce the
103 characteristics and fire detection algorithms of a new global fire product based on FY-3D (recently
104 downloadable from our official website <http://satellite.nsmc.org.cn/portalsite/default.aspx>).
105 Through visual check, consistence check and accuracy assessment based on ground-truth data, FY-3D
106 global fire product is comprehensively compared with the MODIS global fire product at the global and
107 regional scale. Thanks to its good global consistence and regional suitability, FY-3D global fire product
108 has the potential to serve as a continuity of the global MODIS fire product and better support ecological
109 and environment research in China.

110 **2 The overview of FY-3 fire products**

111 **2.1 Instrument**

112 As one of the core instruments of the Fengyun-3 (FY-3) satellite, the updated medium resolution spectral
113 imager (MERSI) has become one of the most advanced remote sensing instruments based on wide swath
114 imaging. FY-3D satellite was launched in November 2017 with 10 sets of remote sensing instruments,
115 including the medium resolution spectral imager (MERSI- II). MERSI- II integrates the functions of the

116 original two imaging instruments (MERSI-I and VIRR) of FY-3B and FY-3C, with a total of 25 channels,
 117 including visible light, near infrared, medium infrared, and far infrared (As Table 1). The infrared
 118 imaging, detection sensitivity, and calibration accuracy of MERSI- II are improved greatly. It is the first
 119 imaging instrument that can access the 250-meter resolution infrared split-window area globally and
 120 capture seamless 250-meter resolution true color global images on a daily basis. MERSI- II also enables
 121 the high-quality retrieval of atmospheric, land, and marine parameters such as clouds, aerosols, vapor,
 122 land surface features, and ocean color, supporting global support for environment and climate issues.

123 **Table 1** Major channel parameters of FY-3D/MERSI- II (Compared with MODIS/Aqua)

| Channel | | Wavelength/ μm | | Waveband | | Resolution/km | | Application |
|---------|-------|---------------------------|--------|-----------------|-------|---------------|-------|----------------------------|
| MERSI | MODIS | MERSI | MODIS | MERSI | MODIS | MERSI | MODIS | |
| 1 | 3 | 0.470 | 0.469 | Visible light | | 0.25 | 0.50 | Ocean Color/ |
| 2 | 4 | 0.550 | 0.555 | Visible light | | 0.25 | 0.50 | Land |
| 3 | 1 | 0.650 | 0.645 | Visible light | | 0.25 | 0.25 | Land/Cloud Ocean |
| 4 | 2 | 0.865 | 0.859 | Near infrared | | 0.25 | 0.25 | Color/Vegetation |
| 5 | 5 | 1.380 | 1.380 | Near infrared | | 1.00 | 0.50 | Land/Cloud/ |
| 6 | 6 | 1.640 | 1.640 | Near infrared | | 1.00 | 0.50 | Snow |
| 7 | 7 | 2.130 | 2.130 | Near infrared | | 1.00 | 0.50 | Land/Cloud |
| 8 | 8 | 0.412 | 0.412 | Visible light | | 1.00 | 1.00 | |
| 9 | 9 | 0.443 | 0.443 | Visible light | | 1.00 | 1.00 | |
| 10 | 10 | 0.490 | 0.488 | Visible light | | 1.00 | 1.00 | |
| 11 | 12 | 0.555 | 0.555 | Visible light | | 1.00 | 1.00 | Ocean Color/ |
| 12 | 13 | 0.670 | 0.667 | Visible light | | 1.00 | 1.00 | Phytoplankton/ |
| 13 | — | 0.709 | — | Visible light | | 1.00 | — | Biogeochemistry |
| 14 | 15 | 0.746 | 0.748 | Visible light | | 1.00 | 1.00 | |
| 15 | 16 | 0.865 | 0.869 | Near infrared | | 1.00 | 1.00 | |
| 16 | 17 | 0.905 | 0.905 | Near infrared | | 1.00 | 1.00 | Atmosphere/ |
| 17 | 18 | 0.936 | 0.936 | Near infrared | | 1.00 | 1.00 | Water Vapor |
| 18 | 19 | 0.940 | 0.940 | Near infrared | | 1.00 | 1.00 | |
| 19 | 26 | 1.040 | 1.040 | Near infrared | | 1.00 | 1.00 | Cirrus |
| 20 | 20 | 3.800 | 3.750 | Medium infrared | | 1.00 | 1.00 | Surface/Cloud/ |
| 21 | 23 | 4.050 | 4.050 | Medium infrared | | 1.00 | 1.00 | Atmospheric Temperature |
| 22 | 28 | 7.200 | 7.325 | Far infrared | | 1.00 | 1.00 | Water Vapor |
| 23 | 29 | 8.550 | 8.550 | Far infrared | | 1.00 | 1.00 | |
| 24 | 31 | 10.800 | 11.030 | Far infrared | | 0.25 | 1.00 | Surface/Cloud |
| 25 | 32 | 12.000 | 12.020 | Far infrared | | 0.25 | 1.00 | Temperature |

124 2.2 Product overview

125 There are two middle-infrared band (3.8um and 4.05um) and both middle-infrared band (3.8um and
126 4.05um) are sensitive to strong heat signals. Their differences lie in their performance under different
127 temperature and radiation conditions. 3.8um is more close to the wavelength of solar radiation, and has
128 better reflection under solar radiation. As a comparison, 4.05um is more easily to miss weak fires.
129 Therefore, current FY-3D fire products are mainly produced based on 3.8um band for better fire
130 identification. According to the calculation, the emissivity of forest and grassland fires in the mid-infrared
131 band can be hundreds of times higher than that of the surface at normal temperature, making the radiance
132 and brightness temperature of the fire-spot significantly higher than surrounding pixels. For rapid
133 monitoring of global wildfires, it is necessary to develop an algorithm for the automatic identification of
134 fire spots.

135

136 MERSI-II fire monitoring products from FY-3D satellite can provide fire spot location, sub-pixel fire
137 spot area, temperature, and fire spot intensity, in inland areas around the world and generate global fire-
138 spot pixel information (including day and night) in an HDF format. FY-3D fire products are produced
139 following a projection with the equal latitude and longitude (0.01 °). Fire spot intensity is classified
140 according to sub-pixel fire spot area and temperature, with an overall accuracy above 85%. Based on
141 daily monitoring products, SMART (Satellite Monitoring Analyzing and Remote sensing Tools) system
142 can generate the images of global monthly fire spot distribution, with a resolution of 0.25 °.

143

144 The algorithm for fire spot identification depends on the sensitivity of mid-infrared channels to high-
145 temperature heat sources. The radiance and brightness temperature of the pixels in the mid-infrared
146 channels with sub-pixel fire spots are higher than those of the surrounding non-fire pixels and those of
147 the pixels in the far-infrared channels. Therefore, the pixels with fire spots can be identified by setting
148 an appropriate threshold, and the estimation of background temperature is the key to high detection
149 accuracy and sensitivity.

150

151 Sub-pixel fire spot estimation relies on the brightness temperature in mid-infrared channels, and the far-
152 infrared channels are employed when the mid-infrared channels have saturated brightness temperature.
153 In the single-channel estimation formula, the temperature of the open flame spot is set to 750 K.

154

155 Fire spot intensity, namely fire radiation power (FRP), is obtained by substituting the area and
156 temperature of sub-pixel fire spots into the Stephen–Boltzmann formula of full-band blackbody radiation.

$$157 J^* = \varepsilon\sigma T^4, \quad (1)$$

158

159 The radiant emittance J^* has dimensions of energy flux, and the SI units of measure are joules per second
160 per square meter. The SI unit for absolute temperature T is the kelvin. ε is the emissivity for the grey
161 body; if it is a blackbody, $\varepsilon = 1$. σ is the Stephen–Boltzmann constant.

162

163 FRP is divided into 10 levels, indicating different ranges of radiation intensity and the fire behavior at

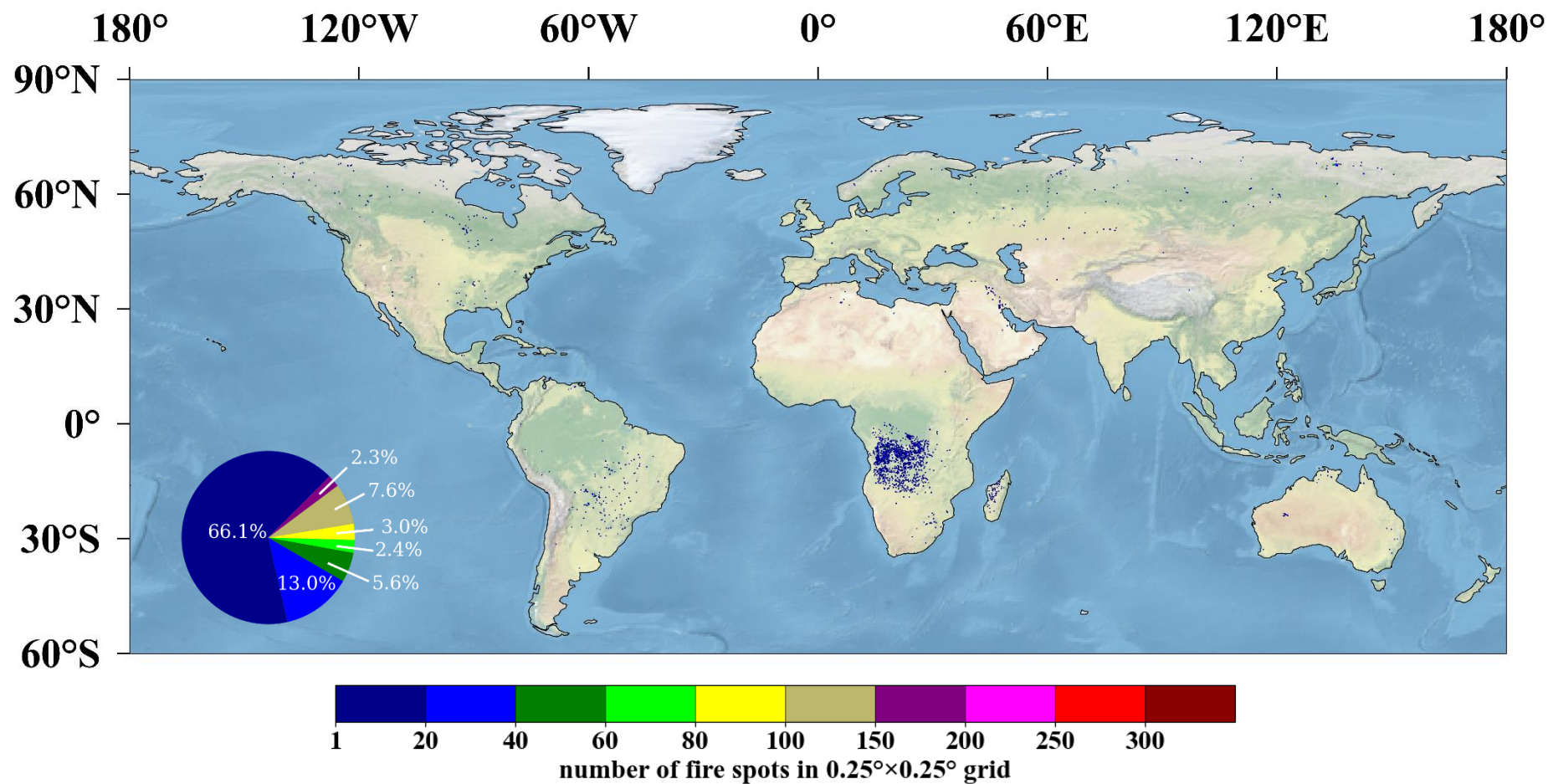
164 fire-spot pixels. Fire spots are classified into four groups with regard to credibility, namely the real fire
165 spots, possible fire spots, fire spots affected by the cloud and noisy (fire spots disturbed by clouds and
166 noise).

167

168 FY-3D/MERSI-II daily global fire monitoring products is illustrated in Fig. 1. The major processing of
169 daily fire spot products is the generation of 5-minute fire spot lists, which includes such information as
170 observation time of fire spot pixels, latitude and longitude, sub-pixel fire spot area and temperature, and
171 FRP. Next, all the 5-minute fire spot information for each day is merged into the daily global fire
172 information list.

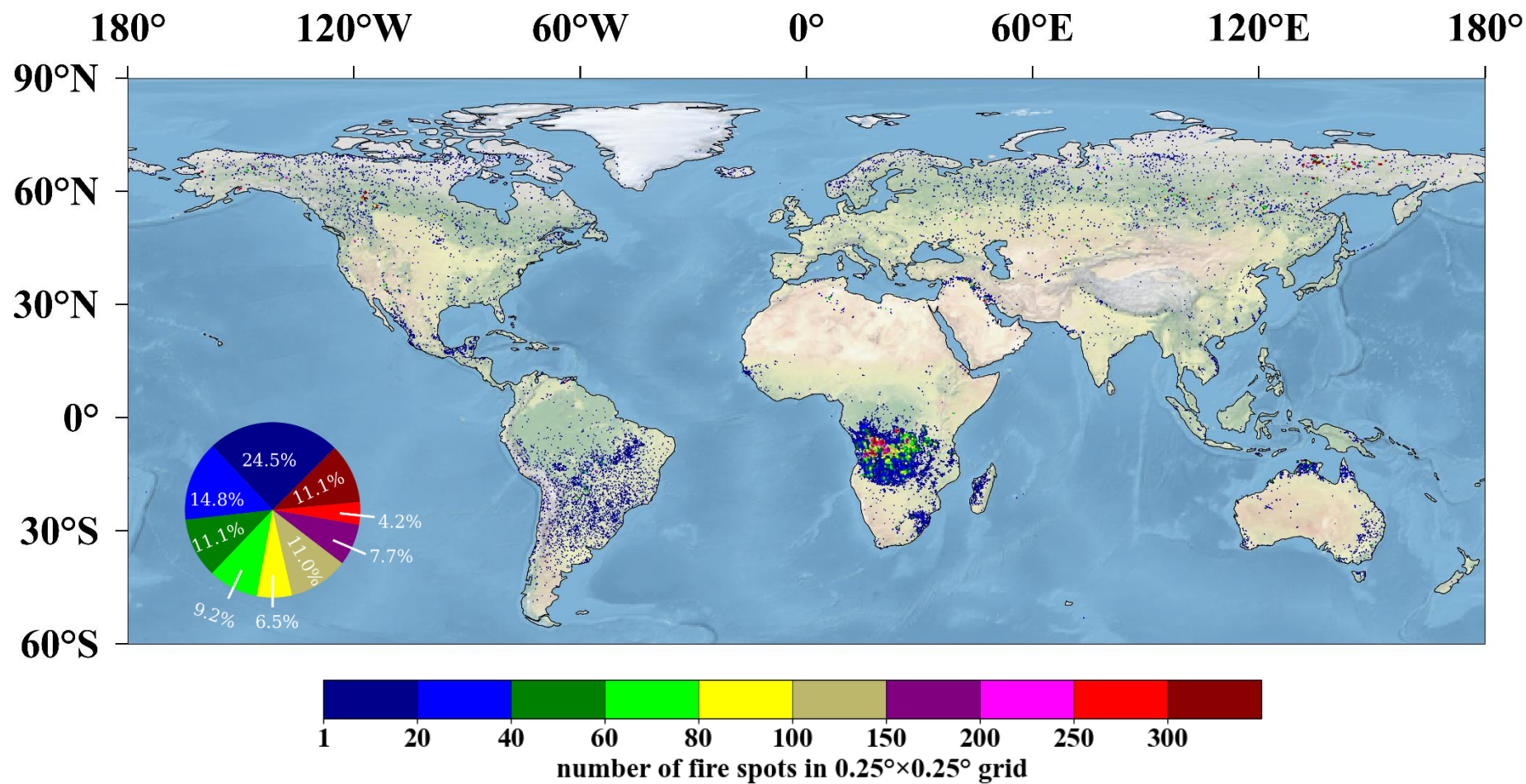
173

174 FY-3D/MERSI-II monthly global fire monitoring products consist of the information list of global fire
175 spot pixels and the density map of global fire spots. The information list of monthly global fire spots
176 covers all global fire spot pixels in this month. Concerning the multi-time monitoring information of the
177 same pixel, the maximum fire spot area is taken as the current-month fire spot information for the pixel.
178 Fig. 2 is an illustration of the density map of global fire spots based on FY-3D/MERSI-II, in which
179 different colors indicate the number of fire spot pixels at $0.25^\circ \times 0.25^\circ$ spatial grid. Compared with daily
180 FY-3D fire products, monthly FY-3D fire products were advantageous of revealing the global patterns of
181 fire spots. As shown in Fig. 2, the global fire spots were mainly distributed in southern Africa, central
182 South America, southern North America, north-central Asia, and northern Australia in June, 2019.



183

184 **Figure 1** Thematic map of global fire monitoring by FY-3D (2019-06-13). The color bar with different colors means the number of fire spots in the 0.25°×0.25° grid.



185

186 **Figure 2** Density map of global fire spots based on FY-3D (2019-06). Fire-prone areas were distributed in northern Russia, south-central Africa, southeastern South America,

187 coastlands of Australia and small parts of Canada.

188 **3 Methods**

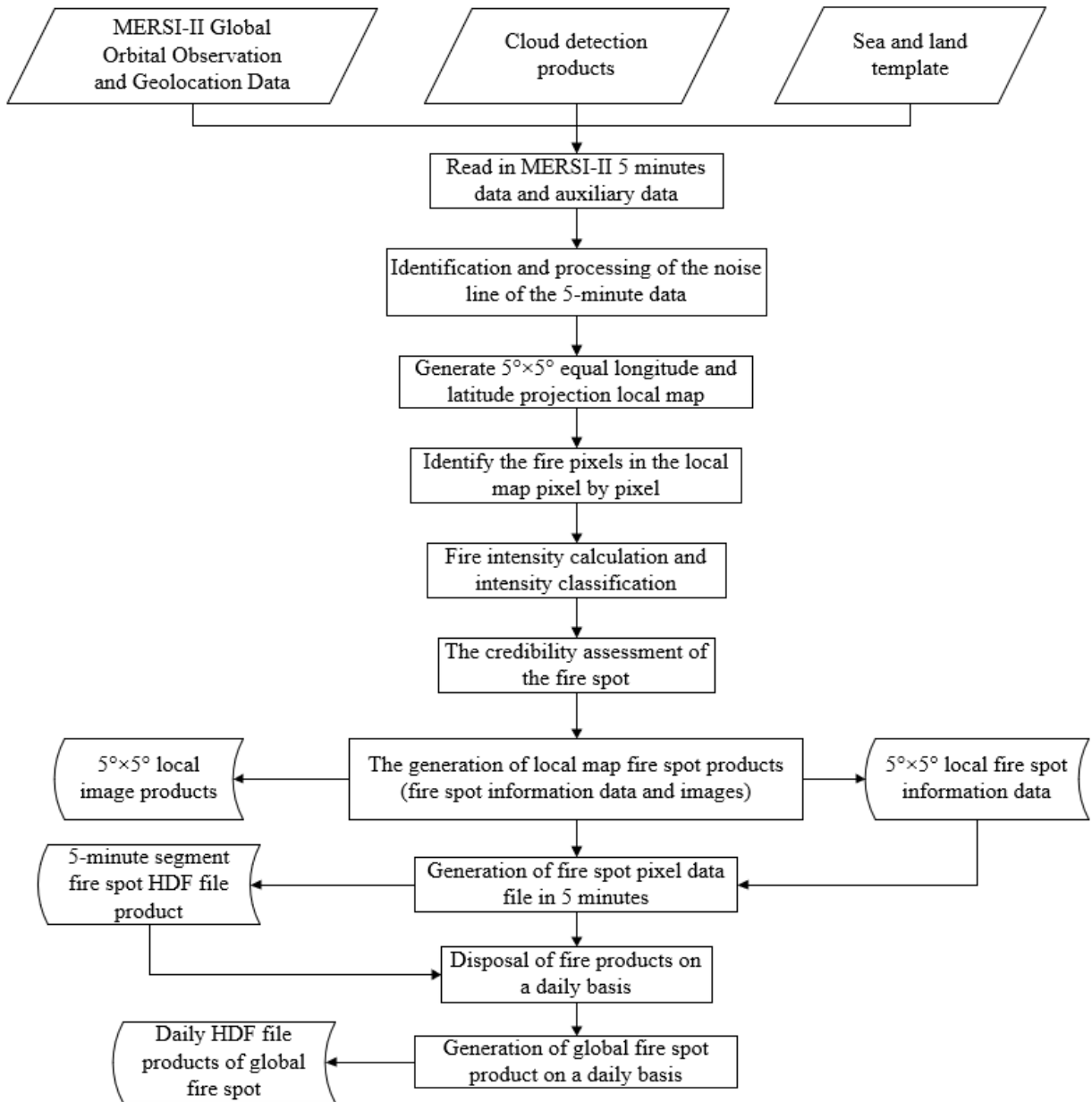
189 This section mainly introduces the specific algorithm and steps for generating FY-3D global fire products
 190 based on the original data obtained from MERSI- II . The input data include MERSI- II global orbital
 191 Earth observations, MERSI- II global orbital geographical locations, MERSI- II global orbital cloud
 192 detection data, and global land and sea template data, as shown in Table 2.

193 **Table 2** Input file list of MERSI- II global fire monitoring software.

| No. | Item | Format | Data type | Period | Source | Description |
|-----|---|--------|-----------|-----------|--|---|
| 1 | MERSI- II global orbital Earth observations | hdf | 1B | Real-time | Preprocessor | Data file after preprocessing 5-minute data segments of MERSI- II |
| 2 | MERSI- II global orbital geolocations | hdf | Float | Real-time | Preprocessor | Locations after preprocessing 5-minute data segments of MERSI- II |
| 3 | MERSI- II global orbital cloud detection data | hdf | Float | Real-time | Product system | 5-minute cloud detection products of MERSI- II produced by the product system |
| 4 | Global land and sea template data | dat | Grid | Static | Data management and user service subsystem | Global land-sea boundaries |

194
 195 Automatic identification of fire spots is the major step for generating fire products. Firstly, the 5-minute
 196 L1 data segments of MERSI- II and various auxiliary data are read in, and the noise lines are identified
 197 to generate the noise line mark. Next, the 5-minute data segments are projected according to rule of the
 198 equal latitude and longitude, and cut as $5^{\circ} \times 5^{\circ}$ grids to generate a local map.

199
 200 Secondly, fire spots in each $5^{\circ} \times 5^{\circ}$ local map are identified pixel by pixel, subject to the calculation of
 201 sub-pixel fire spot area and the estimation of FRP. According to the credibility, the identified fire spot
 202 pixels are classified into four categories. Subsequently, all the $5^{\circ} \times 5^{\circ}$ local fire spot information in the
 203 5-minute data segments is synthesized to generate fire-spot HDF file products. The general steps for
 204 producing FY-3D fire products is briefly explained in Fig 3 and the detailed procedures are explained as
 205 follow.



206

207 **Figure 3** General flow chart for generating FY-3D MERSI- II fire spot products.

208 **3.1 The general principle of fire detection based on MERSI- II**

209 Channel 20 of FY-3D MERSI- II is mid-infrared, with a wavelength of 3.55–3.95 μm , while Channels
 210 24 and 25 are far-infrared, with a wavelength of 10.3–11.3 μm and 11.5–12.5 μm , respectively. According
 211 to Wien's displacement law,

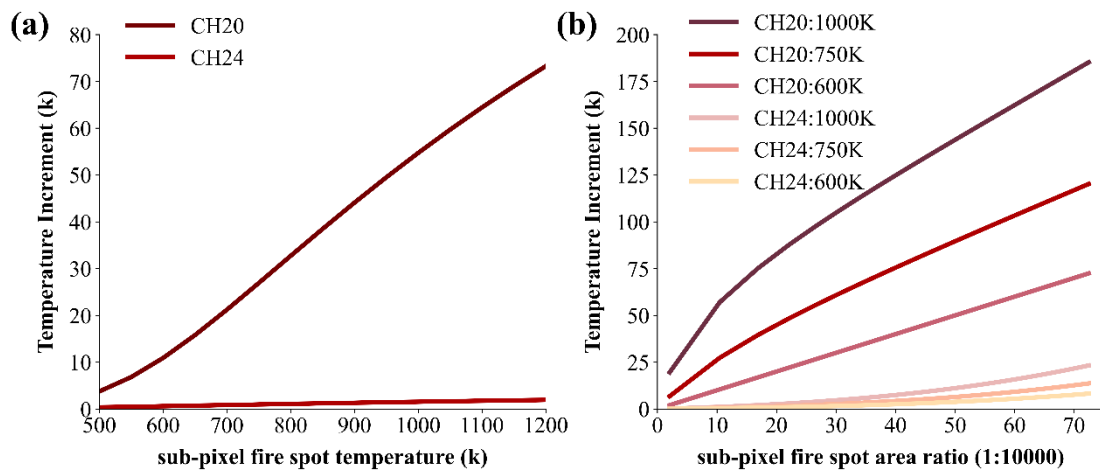
212
$$\lambda * T = b , \tag{2}$$

213 where λ is the peaks at the wavelength, T is the absolute temperature, b is a constant of proportionality
 214 called Wien's displacement constant, equal to about 2898 $\mu\text{m} \cdot \text{K}$. Blackbody temperature T is inversely
 215 proportional to peak radiation wavelength λ_{max} , as the higher temperature can lead to the smaller peak
 216 radiation wavelength. The peak radiation wavelength of the surface at normal temperature (about 300 K)

217 is close to that of Channels 24 and 25; the combustion temperature of forest fires is generally 500 K–
 218 1200 K, and the peak wavelength of thermal radiation is close to that of Channel 20. When a fire spot
 219 appears in the observed pixel, the radiance increment in Channel 20 caused by the high temperature in
 220 the small sub-region of the pixel, where the fire spot is located (Since the pixel resolution of the scanning
 221 radiometer is 1.1 km, it is usually not be all open flame areas at the same time in such a large range), is
 222 much higher than surrounding pixels without an open flame and also greater than that in Channels 24
 223 and 25. In this case, the weighted average of radiance increase and brightness temperature increase of
 224 each channel differ notably in this pixel, based on which the fire information can be extracted and
 225 analyzed.

226

227 As indicated by Fig. 4(a), when the fire spot temperature grows, the brightness temperature of CH20
 228 pixels increases rapidly. Even if the fire spot only accounts for 0.1% the pixel area, the brightness
 229 temperature increment can reach 10 K (44K) when the fire spot is 500 K (900 K). Although the brightness
 230 temperature increase of CH24 also rises with the higher fire spot temperature, it is far lower than that of
 231 CH20. Fig. 4(b) illustrates that as the fire spot area gets larger, the brightness temperature of CH20-
 232 mixed-pixels grows rapidly. It reaches 12K when the fire spot is 900 K, even if the fire spot only accounts
 233 for 0.01% of the pixel area. Similarly, the brightness temperature increment of CH24 grows at a much
 234 lower rate than CH20.



235

236 **Figure 4** (a): Curves of FY-3D/MERSI- II CH20 and CH24 brightness temperature increment with fire
 237 spot temperature (with fire spot area accounting for 0.1% of pixel area and background temperature at
 238 290 K). (b): Curves of FY-3D/MERSI- II CH20 and CH24 brightness temperature increment with fire
 239 spot area (with fire spot temperature at 600 K, 750 K, and 1000 K, background temperature at 290 K,
 240 and the ratio of fire spot area to pixel area increasing from 0.01% to 0.4%).

241 3.2 Automatic identification algorithms for fire spots

242 3.2.1 Detection of cloud pixels

243 Effective cloud detection is required for generating reliable fire products for the following reasons. Firstly,
 244 the existence of cloud in the atmospheric layers may block the emitted information of fire spots, leading
 245 to missed identification. Secondly, specular reflection of cloud can lead to wrong identification of fire

246 spots. Therefore, cloud identification was conducted before fire identification. Similar to MODIS, FY-
 247 3D also included radiation information from multiple bands and the principle of cloud identification for
 248 FY-3D fire products was similar to that of MODIS. Based on the reflectance difference between cloud
 249 and land pixels, we classified cloud pixels following the rules listed in Table 3.

250

251 **Table 3** Major rules for cloud pixel identification.

| number | conditions |
|--------|--|
| 1 | $T_{Mir} - T_{far1} < 4K$ |
| 2 | $T_{Mir} - T_{far1} > 20K \ \& \ T_{Mir} < 285K \ \ T_{far1} < 280K$ |
| 3 | $R_{Vis} > 0.28 \ \& \ SolarZenith < 70^\circ \ \ SolarZenith < 60^\circ \ \& \ SateZenith < 60^\circ$ |
| 4 | $T_{far1} < 265K$ |
| 5 | $T_{Mir} < 270K \ \& \ T_{far1} - T_{far2} < 4K$ |
| 6 | $T_{far1} < 270K \ \& \ T_{far1} - T_{far2} > 60K$ |
| 7 | $T_{Mir} < 320K \ \& \ T_{Mir} < T_{Mir_TH}$ |
| 8 | $SolarZenith > 70 \ \& \ R_{Vis} > 0.28 \ T_{Mir} < 320K$ |

252 T_{Mir} : Mid-infrared channel; T_{far1} : 10.8um Far-infrared channel; T_{far2} : 12um Far-infrared channel; R_{Vis} :
 253 Visible light channel; SolarZenith: Solar zenith angle; SateZenith: Satellite zenith angle.

254 Note: These eight rules are set to exclude a diversity of cloud bias. And a pixel that meets any rule
 255 any rule in Table

256

257 3.2.2 Calculation of background temperature

258 According to the principle of fire spot identification, when a fire spot appears in a pixel (i.e., open flame),
 259 the brightness temperature of the pixel in Channel 20 is significantly higher than the background
 260 brightness temperature (the brightness temperature of surrounding non-fire pixels); the brightness
 261 temperatures of Channels 24 and 25 are also higher than the background, but the temperature difference
 262 is much smaller than Channel 20. In this case, the difference of brightness temperature between fire-spot
 263 pixels and background in both the mid-infrared channel and far-infrared channels can be employed as
 264 important factors for automatic identification of fire spots. Therefore, the background temperature of the
 265 detected pixel is required for identifying fire spots. Since the background temperature cannot be obtained
 266 from the fire-spot pixels, it should be calculated according to the average of their surrounding pixels.
 267 However, the reflection of solar radiation during the daytime also causes a higher brightness temperature
 268 in the mid-infrared channel, which mainly occurs in the zone bare of vegetation, cloud surface, and water
 269 bodies (specular reflection). In particular, the difference of brightness temperature between mid-infrared
 270 and far-infrared channels caused by specular reflection of solar radiation can reach tens of K on the cloud
 271 surface and water bodies. Since the reflection of solar radiation on the bare surface is relatively weak in
 272 the mid-infrared channel, a few degrees of difference can cause non-fire pixels misclassified as fire pixels,
 273 due to the high sensitivity requirement for fire identification. When the background brightness
 274 temperature is calculated, pixels that already contain fire spots should also be excluded. Therefore,

275 suspected high-temperature pixels, which may already contain fire spot pixels, cloudy pixels, water
276 pixels and those pixels affected by solar flare should be removed for background temperature calculation.

277

278 Furthermore, the pixel size in the mid-infrared channel of a meteorological satellite is about 1 km². Within
279 this range, the underlying surface may be diversified and composed of sub-regions with different
280 fractional vegetation cover (FVC). In the daytime, affected by solar radiation, the brightness temperature
281 of different FVC may vary, making the calculated background temperature higher than expected. To
282 address this issue, Kaufman et al. (1998) suggested the use of standard deviation of background
283 temperature for fire identification, which significantly reduced the overestimation of background
284 temperature caused by different underlying surfaces.

285

286 After above-mentioned disturbing pixels were removed, the average and standard deviation of
287 background temperature in the mid-infrared channel, and the background average and standard deviation
288 of brightness temperature difference between the mid-infrared and far-infrared channels were calculated
289 with peripheral pixels as background pixels.

290

291 The calculation of background temperature was acquired in the following steps. For each 3×3 window,
292 the background temperature is calculated as the mean temperature of all background pixels. Suspicious
293 high-temperature pixels can be identified according to the following conditions:

$$294 \quad T_{Mir} > T_{th} \text{ Or } T_{Mir} > T'_{Mir_bg} + \Delta T_{Mir_bg}$$

295 Where T_{Mir} is the bright temperature in the middle-infrared channel. T_{th} is the threshold for high-
296 temperature pixels in the middle-infrared channel, usually set as sum of the mean bright temperature of
297 all pixels in the window and 2 × its corresponding standard deviation. T'_{Mir_bg} is the mean bright
298 temperature of background pixels.

299

300 ΔT_{Mir_bg} is the allowed difference between the mean background bright temperature and the suspicious
301 high-temperature pixel, usually set as 2.5 × standard deviation of background pixels. If there were less
302 than 20% of pixels were cloudless pixels, then the 3 × 3 window was extended to 5 × 5, 7 × 7, 9 × 9...51 ×
303 51. If still not applicable, then this pixel was marked as a non-fire pixel.

304 **3.2.2 Identification of fire pixels**

305 With obtained background temperature, the difference between brightness temperature and background
306 temperature in the mid-infrared channel, as well as the difference of brightness temperature and
307 background temperature between mid-infrared and far-infrared channels, at the candidate pixels could
308 be calculated, based on which we could decide whether the threshold of fire spot identification was
309 reached. If the threshold was reached, the pixel will be preliminarily marked as a fire pixel. Next, for
310 daytime observation data, it is necessary to further check whether the increase of brightness temperature
311 in the mid-infrared channel was interfered by solar radiation in the cloud area. Through the two-stage
312 check, fire pixels could be effectively extracted.

313

314 When the following two conditions are met, a pixel can be identified as fire pixel:

315 (1) $T_{3.9} > T_{3.9bg} + n_1 \times \delta T_{3.9bg}$

316 (2) $\Delta T_{3.9_11} > \Delta T_{3.9bg_11bg} + n_2 \times \delta T_{3.9bg_11bg}$

317 Where $T_{3.9}$ is the bright temperature of the pixel at 3.9 μm . $T_{3.9bg}$ is the background bright temperature.
318 $\delta T_{3.9bg}$ is the standard deviation of bright temperature of background pixels. $\Delta T_{3.9_11}$ is the difference of
319 bright temperature between 3.9 μm and 11 μm . $\Delta T_{3.9bg_11bg}$ is the difference of background bright
320 temperature between 3.9 μm and 11 μm . The setting of this condition aimed to identify the difference of
321 land cover types in the window. When the land cover types in the window were generally consistent,
322 $\delta T_{3.9bg_11bg}$ is relatively small. For the identification of fire pixels, when $\delta T_{3.9bg_11bg}$ was smaller than 2k,
323 this value was replaced using 2K. When $\delta T_{3.9bg_11bg}$ was larger than 4k, this value was replaced using 4K.
324 n_1 and n_2 are background coefficients, which varies across regions, observation time and observation
325 angles. For instance, for Northern grasslands, n_1 and n_2 was set as 3 and 3.5, respectively.

326 3.2.3 Identification of noise line

327 Satellite data received by the ground system contain noise. For instance, some scanning lines may contain
328 many noisy pixels that affect fire spot identification. In this case, noise lines, referred to multiple
329 consecutive noisy pixels in one scanning line, should be checked firstly. Since the identification of fire
330 was carried out on the areal map projected with an equal latitude and on the same circle of longitude, the
331 identified latitude and longitude of fire spots failed to reflect the original positions of scanning lines.
332 Therefore, the noise line was identified on the 5-minute data segments before projection. Firstly, the 5-
333 minute data segments were employed to identify fire spots, and the line number of identified fire spot
334 pixels was recorded. Following this, the number of fire spot pixels in each line was counted. When the
335 number of fire spot pixels in a line exceeded the empirical threshold, it was identified as a noise line, and
336 all pixels in the line are marked as noisy ones. In the following process, all pixels in this line were no
337 longer considered for fire-spot identification.

338 3.3 Estimation of fire radiation power (FRP)

339 FRP can be calculated using Stephen-Boltzmann formula (Matson et al., 1984) through the estimation
340 of sub-pixel fire spot area and temperature.

341 3.3.1 Estimation of sub-pixel fire spot area and temperature

342 MERSI-II data is 12 bits, with a quantization level of 0–4095 and high radiation resolution. The spatial
343 resolution is 1.1 km, and the radiance of a pixel observed by the satellite is the weighted average of the
344 radiance of all the ground objects within the pixel range, as

345
$$N_t = (\sum_{i=1}^n \Delta S_i N_{Ti}) / S, \quad (3)$$

346 where N_t is the radiance of the pixel observed by the satellite; t is the brightness temperature
347 corresponding to N_t ; ΔS_i is the area of the i^{th} sub-pixel; N_{Ti} is the radiance of the sub-pixel; T_i is the
348 temperature of the sub-pixel; S is the total area of the pixel.

349

350 Due to different FRP and temperature, underlying surfaces containing fire spots can be divided into fire

351 zones and non-fire zones (background). When fire spots appear, the radiance of pixels containing fire
352 spots (i.e. mixed pixels) can be expressed by the following formula:

353

$$354 \quad N_{mix} = P * N_{hi} + (1 - P) * N_{bg} = P * \frac{C_1 V_i^3}{e^{T_{hi}} - 1} + (1 - P) * \frac{C_1 V_i^3}{e^{T_{bg}} - 1}, \quad (4)$$

355 where P is the percentage of sub-pixel fire spot area in the pixel; N_{mix} , N_{hi} , and N_{bg} are the radiance of
356 mixed pixels, sub-pixel fire spot (fire zone) and surrounding background; T_{hi} and T_{bg} are the temperature
357 of sub-pixel fire spots and background; V_i is the central wavenumber of channels; C_1 and C_2 are Planck
358 constants.

359

360 For Eq. (4), there are two unknown variables, P and T_{hi} . According to the characteristics of infrared
361 channels in the scanning radiometer (dynamic brightness temperature and spatial resolution), the
362 radiation increase of high-temperature sources varies notably in different bands. To address this issue, a
363 strategy is employed to estimate the actual area and temperature of fire spots according to the radiation
364 in different infrared channels. When the mid-infrared channel was not saturated, it was used for
365 estimating the sub-pixel fire spot area and temperature. Otherwise, the far-infrared channel was
366 alternatively employed for estimation.

367

368 When a single channel was adopted to estimate the sub-pixel fire spot area, the fire spot temperature was
369 set to an appropriate value, which was 750 K in this product.

370 **3.3.2 Calculation of fire radiation power**

371 Based on the percentage of sub-pixel fire spot area, P , and fire spot temperature, FRP can be calculated
372 using Stephen–Boltzmann formula:

$$373 \quad FRP = P * S_{\lambda,\varphi} * \sigma T^4, \quad (5)$$

374 where

375 FRP is fire radiation power, W;

376 $S_{\lambda,\varphi}$ is the sub-pixel fire spot area of pixels located at longitude λ and latitude φ , which is calculated
377 according to the percentage of sub-pixel fire spot area P and the total pixel area;

378 T is the sub-pixel fire spot temperature and set to 750 K;

379 σ is Stephen–Boltzmann constant, 5.6704×10^{-8} (W m⁻² K⁻⁴).

380 **3.4 Verification methods**

381 Wildfires are characterized by random and rapid changes, so it is difficult to verify the product accuracy
382 of GFR (Global Fire) according to actual ground information. In this paper, the accuracy of FY-3 fire
383 products is tested through visual interpretation and cross-verification of other products. Specifically, due
384 to the extreme large size of GFR datasets, we set the different strategies for accuracy assessment. For
385 visual interpretation, several 5-minute data segments with regional representation were selected for
386 verification using manually identified fire spots; For cross-verification with other fire products, global
387 fire spot data throughout 2019 were employed.

388

389 The error was defined as the distance from the positions (longitude and latitude) of automatically
390 identified fire spot pixels to corresponding manually identified ones. When the difference in latitude and
391 longitude was less than or equal to 0.02° , the automatically identified pixel was regarded as a successful
392 identification.

$$393 \quad \sqrt{(lat1 - lat2)^2 + (long1 - long2)^2} \leq 0.02^\circ$$

394 where $lat1$ and $lat2$ are the latitude of PGS (Product Generation System) fire spot pixels and manually
395 identified pixels (reference pixels); $long1$ and $long2$ are the longitude of PGS fire spot pixels and
396 manually identified pixels (reference pixels), respectively.

397

398 In addition to the visual-check based accuracy assessment at the global scale, we also employed a set of
399 field collected reference data to verify the suitability of FY-3D in China, which is further explained in
400 the following sections.

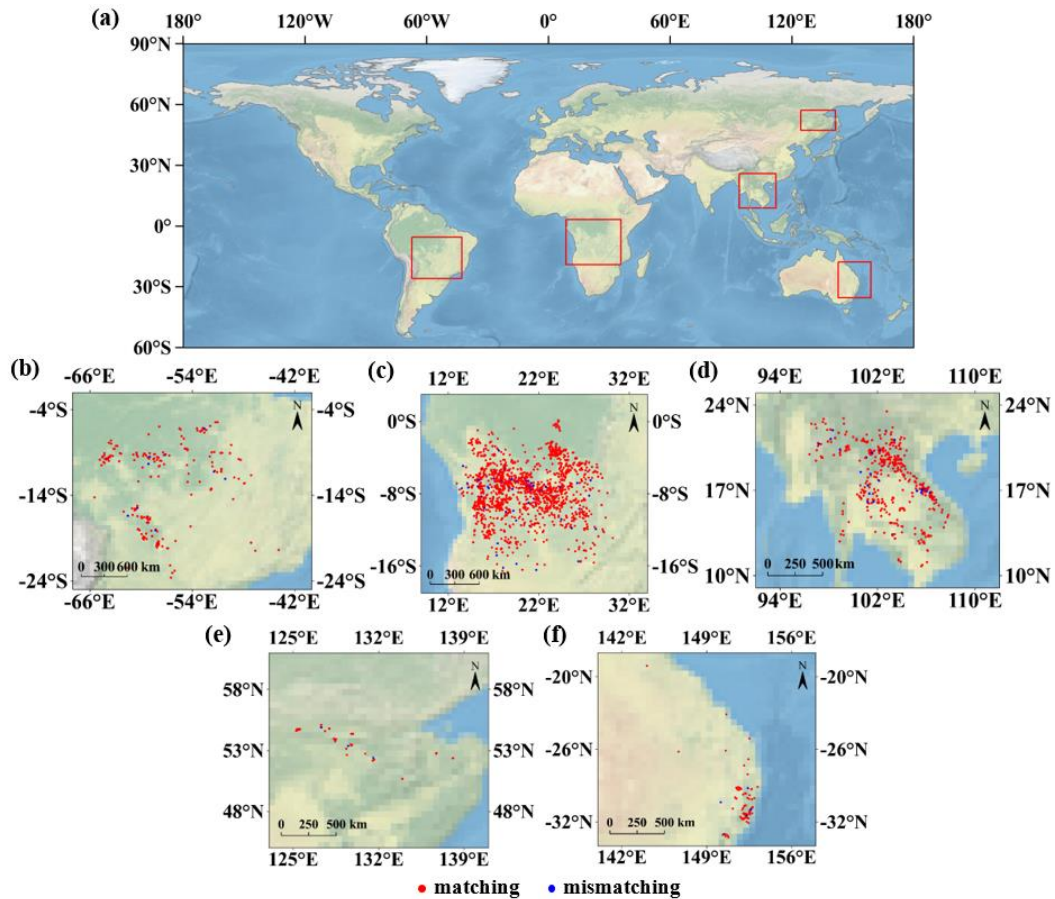
401 **4 Results**

402 **4.1 Global accuracy assessment of FY-3D fire products based on visual interpretation**

403 In this research, 5-minute segments of FY-3D fire products in different continents, including Africa,
404 South America, Indo-China Peninsula, Siberia and Australia were collected at 12:15 (UTC) on June 13,
405 2018, 17: 05 (UTC) on August 21, 2019, 06:15 (UTC) on March 13, 2019, 03:40 (UTC) on November
406 13, 2019, 17:40 (UTC) on May 29, 2018 respectively for visual interpretation. The specific observation
407 positions are shown in Fig. 5 with five corresponding fire detection pictures of FY-3D.

408

409 These regions were selected for evaluating the global reliability of FY-3D fire products for the following
410 reasons. Firstly, Africa, South America, Indo-China Peninsula, Siberia and Australia are the regions with
411 the most frequent fire events across the globe. Secondly, there are rich vegetation in these regions, which
412 provides the foundation for stable combustion across a year. Thirdly, these regions cover large area with
413 generally unified underlying surfaces. Fourthly, these areas are of regional representation: Siberia
414 represents typical regions with frequent forest fires in Northern Hemisphere. Africa represents typical
415 tropical grasslands and forests in the equator regions. South America represents virgin tropical rainforests.



416

417 **Figure 5** (a), Observation positions from FY-3D MERSI- II . The red frame at the upper right shows FY-
 418 3D MERSI- II is located at the border between Northeast China and Russia. The lower left red frame
 419 shows FY-3D MERSI- II is over east-central South America and the central red frame shows FY-3D
 420 MERSI- II is located in south-central Africa. The middle right red frame shows the FY-3D MERSI- II is
 421 over Indo-China Peninsula and the lower right red frame shows the FY-3D MERSI- II is located in east
 422 Australia. (b)-(f), Fire spot matching diagram between GFR and visual interpretation data of FY-3D
 423 MERSI- II . The red points indicate that GFR matches visual interpretation data, and the blue points
 424 represent that only GFR recognized the fire spots, which was not.

425

426 Fig. 5 presents the spatial distribution of GFR fire spots and manually identified fire pixels in the 5-
 427 minute segment of the above regions. According to Fig 5b, most fire spots in FY-3D products and
 428 manually extracted fire spots in South America were in same positions. In Fig 5c, most FY-3D and
 429 manually extracted fire spots in Africa coincided or were in a close position. In Fig 5d, despite a few
 430 mismatched fire spots, the position of FY-3D and manually extracted fire spots in Indo-China Peninsula
 431 was consistent. Fig 5e and Fig 5f also show that most fire spots are matched in Russia and Australia.
 432 Table 4 shows accuracy of GFR fire spots in the five typical regions. The accuracy of automatically
 433 identified fire spot in all regions was generally consistent and all exceeded 90%. Since these selected
 434 regions represented distinct vegetation types and located in different hemispheres, the verification of FY-
 435 3D fire products based on 0.24 SMART proved its stability and reliable high-accuracy at the global scale.
 436

437 It is worth mentioning that the visual-check based accuracy assessment mainly considered the
 438 commission error, while omission error cannot be effectively revealed for the following reason. The
 439 omitted fires were mainly caused by the requirement of minimum burning area. Since the spatial
 440 resolution of FY-3D and MODIS active fire products is 1km, small fires (less than 100m²) could not be
 441 captured by sensors and recognized through visual check. Meanwhile, the thermal abnormalities at the
 442 edge of cloud and water bodies, which could be recognized through visual check. In this case, the visual-
 443 check based accuracy assessment mainly considered the commission errors.

444

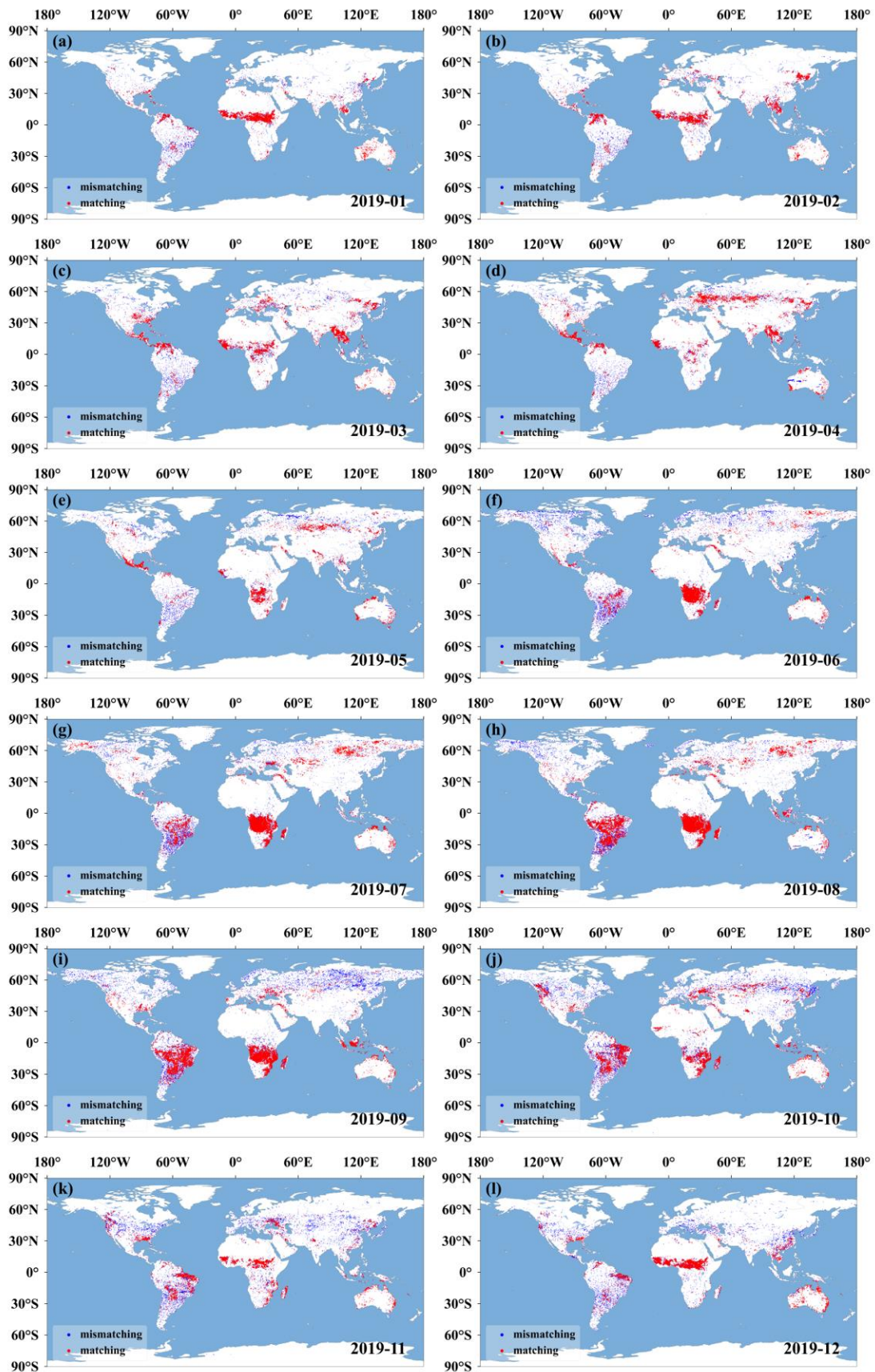
445 **Table 4** Accuracy assessment of FY-3D identified fires based on SMART (Visual check)

| Region | GFR-based fire spots | Not match with SMART | Accuracy (%) |
|----------------------------|----------------------|----------------------|--------------|
| South-central Africa | 1429 | 77 | 94.6 |
| East-central South America | 204 | 12 | 94.1 |
| Siberia | 32 | 3 | 90.6 |
| Australia | 85 | 7 | 91.8 |
| Indo-China Peninsula | 438 | 32 | 92.7 |
| Overall | 2188 | 131 | 94.0 |

446 **4.2 Cross-verification between FY-3D and MODIS global fire products**

447 The cross-verification between FY-3D fire products and the mainstream MODIS fire products,
 448 MYD14A1 V6 (<https://firms.modaps.eosdis.nasa.gov/map/>) with a daily temporal resolution and 1km
 449 spatial resolution was conducted using the entire 2019 datasets. The data sets with observation time less
 450 than 1 h were selected; the underlying surfaces were visually checked to remove areas covered by non-
 451 vegetation such as water, ice and snow, and bare land. According to the criterion that the distance
 452 matching between the two fire spot pixels was less than 0.03 °, cross-verification was conducted with
 453 different months, underlying surfaces, regions, and fire intensities. In 2019, there were 2,237,714 fire
 454 spot pixels in MODIS fire products, 1,866,920 of which were matched with FY-3D fire products, with
 455 an overall consistence of 84.4% (as shown in Fig. 6). As shown in Figure 6, global fire spots were mainly
 456 distributed in America, south-central Africa, East, and Southeast Asia, Australia, and parts of Europe,
 457 and there were notable spatiotemporal variations of identified fire spots. Specifically, given the overall
 458 data volume and spatial distribution, the total number of fire spot pixels from MODIS fire products was
 459 larger than FY-3D products. For individual regions, the more fire spots, the higher consistence between
 460 FY and MODIS fire products. Africa is the region with the most fire spots across the globe. From May
 461 to October, a majority of fire spots was located in southern Africa whilst a majority of fire spots from
 462 November to next April was located in the middle and western coastal of Africa. The consistence between
 463 MODIS and FY-3D products was higher than other regions. The distribution of fire spots in South
 464 America also presented seasonal characteristics. From July to October, fire spots mainly concentrated in
 465 middle parts of South America. For other seasons, fire spots in South America mainly concentrated in

466 the North and other parts. The consistence between MODIS and FY-3D fire products also demonstrated
467 seasonal differences, with a high consistence from August to November and a relatively low consistence
468 in other seasons. For Eurasia, there were notable seasonal variations of spatial patterns of fire spots.
469 During March to August, there were relatively many fire spots and the consistence between MODIS and
470 FY-3D fire products was relatively high in this region.



471

472 **Figure 6** The consistence between FY-3D and MODIS fire products in different months (2019)

473

474 In addition to the overall consistence between MODIS and FY-3D fire products, we also conducted cross-
 475 verification between the two global fire products in different months, underlying surfaces, regions and
 476 fire intensities as follows.

477 4.2.1 Cross-verification between MODIS and FY-3D in different months

478 Fig. 7(a) illustrates the monthly consistence between FY-3D and MODIS fire products in 2019. The
 479 consistence in the remaining months is over 80% except that in April, October, and November. The
 480 highest appears in July, exceeding 90%, while the lowest is in April, 71%. Detailed parameters can be
 481 found in Table 5. From the global perspective, the number of fire spots was larger in July, August and
 482 September and the mean consistence between MODIS and FY-3D fire products was larger than 85%. For
 483 July when the fire products were the most, the consistence achieved 90%. From January to May, the
 484 number of fire spots was relatively small, and the mean consistence was around 80%. The consistence
 485 for April was 71%, lowest among all months. The notable monthly variations of the consistence between
 486 MODIS and FY-3D fire products was mainly attributed to the uneven spatial distribution of fire spots
 487 across the globe. As shown in Fig 6, in June and July, a large number of fire spots mainly concentrated
 488 in Africa, South America and Eurasia, leading to a high consistence of fire identification. In April, there
 489 were limited and sparsely distributed fire spots in Africa and South America, leading to a low consistence.
 490 According to the statistics, the number of fire spots was positively correlated with the consistence
 491 between different fire products. Meanwhile, in seasons when fire could last longer, the consistence was
 492 relatively higher.

493 **Table 5** Cross-satellite comparison between FY-3D and MODIS fire products.

| Time | Match | Mismatch | Total | Consistence (%) |
|--------|---------|----------|---------|-----------------|
| 201901 | 70799 | 14188 | 84987 | 83 |
| 201902 | 66849 | 14717 | 81566 | 82 |
| 201903 | 105176 | 22576 | 127752 | 82 |
| 201904 | 94474 | 39250 | 133724 | 71 |
| 201905 | 75703 | 17135 | 92838 | 82 |
| 201906 | 174587 | 33862 | 208449 | 84 |
| 201907 | 362108 | 39683 | 401791 | 90 |
| 201908 | 315182 | 51627 | 366809 | 86 |
| 201909 | 226363 | 47607 | 273970 | 83 |
| 201910 | 115975 | 33956 | 149931 | 77 |
| 201911 | 102240 | 27732 | 129972 | 79 |
| 201912 | 157464 | 28461 | 185925 | 85 |
| Total | 1866920 | 370794 | 2237714 | 83.4 |

494 4.2.2 Cross-verification between MODIS and FY-3D on different underlying surfaces

495 Statistical analysis of consistence is carried out with different types of underlying surfaces. The data of

496 underlying surfaces is the global land use are detailed in Table 6.

497

498 The 15 types of underlying surfaces were selected for verification. Table 6 and Fig. 7(c) shows the
499 consistence of FY-3D and MODIS fire products with different underlying surfaces. From the
500 classification of different underlying surfaces, the remaining types are over 80% except (11) Post-
501 flooding or irrigated croplands (or aquatic), (14) Rainfed crops, (20) Mosaic cropland (50-70%) /
502 vegetation (grassland/shrubland/forest) (20-50%), (140) Closed to open (>15%) herbaceous vegetation
503 (grassland, savannas or lichens/mosses), and (150) Sparse (<15%) vegetation. When the underlying
504 surface is the open (15%–40%) coniferous and deciduous forest or evergreen forest, the consistence is
505 the highest, at 93%. In addition, according to the classification of underlying surfaces, the fire spot
506 identification shows high consistence when the underlying surface is the forest. The consistence between
507 FY-3D and MODIS fire spots on different underlying surfaces in each month was demonstrated in Table
508 7. Clearly, we can found the fluctuation of consistence across seasons due to the variation of combustible
509 vegetation, which influenced the detecting capability of MODIS and FY-3D.

510

511 The low consistence between FY-3D and MODIS fire products was observed for underlying surface 11,
512 14, 20, 140 and 150. Specifically, 11, 14 and 20 could be categorized as farmlands. 140 was mainly
513 occupied by herbaceous vegetation or sparse grasslands. 150 was mainly occupied by sparse grasslands.
514 Generally, these surfaces were all covered by sparse or unstable vegetation, the fire on which can last for
515 a relatively short period. Meanwhile, the observation time lag between FY-3D and MODIS was larger
516 than 30 minutes. Therefore, the consistence of FY-3D and MODIS fire products on these surface types
517 was lower than other surface types.

518

Table 6 Classification of underlying surfaces (land cover types).

| ID | Definition of underlying surfaces |
|-----|---|
| 11 | Post-flooding or irrigated croplands (or aquatic) |
| 14 | Rainfed croplands |
| 20 | Mosaic cropland (50-70%) / vegetation (grassland/shrubland/forest) (20-50%) |
| 30 | Mosaic vegetation (grassland/shrubland/forest) (50-70%) / cropland (20-50%) |
| 40 | Closed to open (>15%) broadleaved evergreen or semi-deciduous forest (>5m) |
| 50 | Closed (>40%) broadleaved deciduous forest (>5m) |
| 60 | Open (15-40%) broadleaved deciduous forest/woodland (>5m) |
| 70 | Closed (>40%) needleleaved evergreen forest (>5m) |
| 90 | Open (15-40%) needleleaved deciduous or evergreen forest (>5m) |
| 100 | Closed to open (>15%) mixed broadleaved and needleleaved forest (>5m) |
| 110 | Mosaic forest or shrubland (50-70%) / grassland (20-50%) |
| 120 | Mosaic grassland (50-70%) / forest or shrubland (20-50%) |
| 130 | Closed to open (>15%) (broadleaved or needleleaved, evergreen or deciduous) shrubland (<5m) |
| 140 | Closed to open (>15%) herbaceous vegetation (grassland, savannas or lichens/mosses) |
| 150 | Sparse (<15%) vegetation |

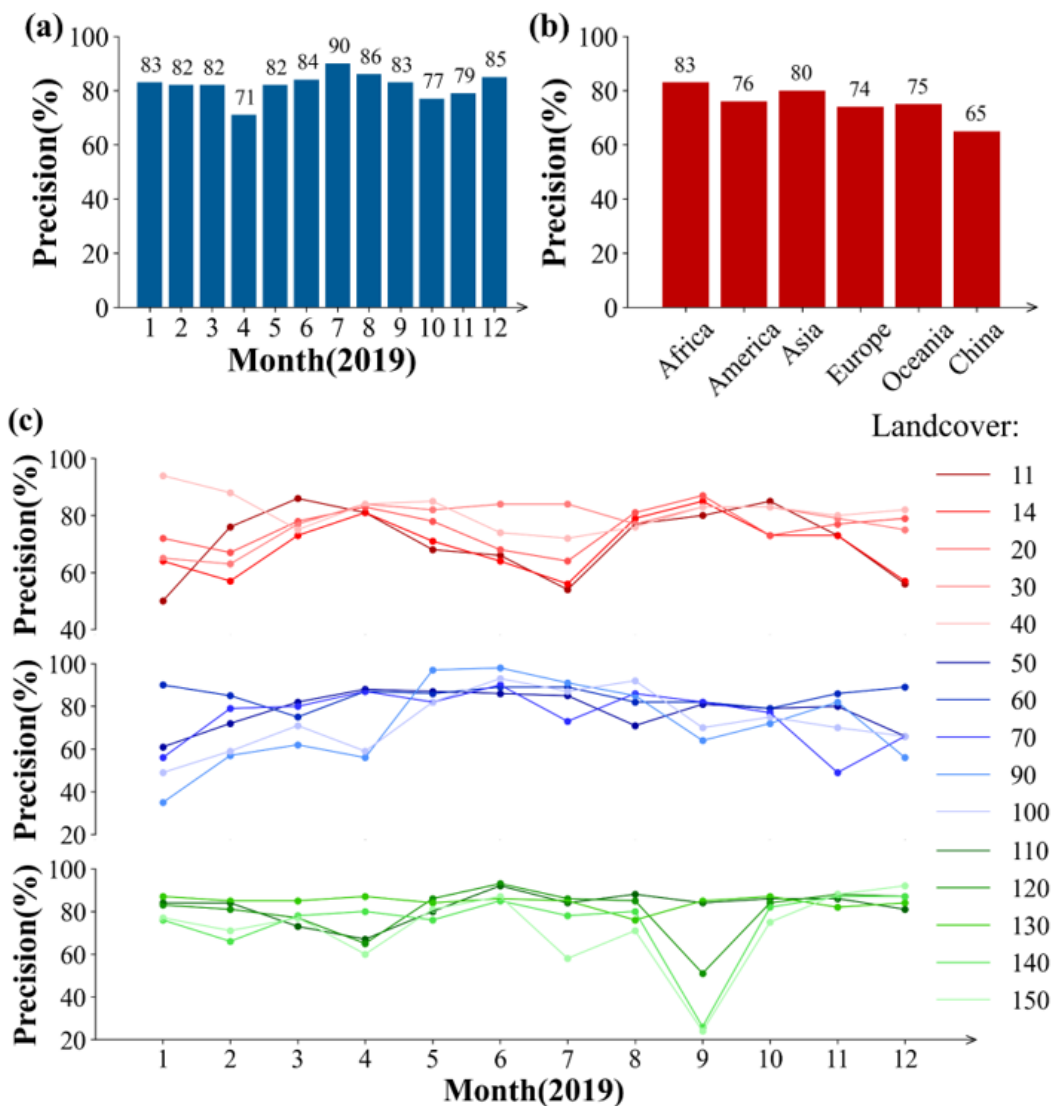
519

520 **Table 7** the consistence between FY-3D and MODIS fire spots on different underlying surfaces in each month (total FY-3D pixels (consistence)).

| ID | Jan | Feb | Mar | Apr | May | Jun | Jul | Aug | Sep | Oct | Nov | Dec |
|-----|------------|------------|------------|------------|------------|-------------|------------|------------|------------|------------|------------|------------|
| 11 | 754 (50%) | 1471(76%) | 1651(86%) | 450(81%) | 201(68%) | 344(66%) | 353(54%) | 678(77%) | 1786(80%) | 1516(85%) | 558(73%) | 416(56%) |
| 14 | 4459(64%) | 5024(57%) | 7745(73%) | 11439(81%) | 6818(71%) | 4137(64%) | 2135(56%) | 4122(79%) | 8090(85%) | 4561(73%) | 3154(73%) | 1663(57%) |
| 20 | 8033(72%) | 8596(67%) | 13513(78%) | 20282(83%) | 14772(78%) | 5216(68%) | 2921(64%) | 5449(81%) | 11970(87%) | 5858(73%) | 4721(77%) | 5572(79%) |
| 30 | 5786(65%) | 7227(63%) | 13018(77%) | 22626(84%) | 26523(82%) | 23024(84%) | 16007(84%) | 6455(77%) | 14534(83%) | 16523(83%) | 8646(79%) | 5199(75%) |
| 40 | 45313(94%) | 38194(88%) | 25315(75%) | 63474(84%) | 69987(85%) | 14770(74%) | 8265(72%) | 7107(76%) | 22921(83%) | 31839(83%) | 14646(80%) | 9556(82%) |
| 50 | 3454(61%) | 8398(72%) | 19960(82%) | 45387(88%) | 51148(87%) | 42981(86%) | 25424(85%) | 4356(71%) | 5481(81%) | 6237(79%) | 3713(80%) | 1920(66%) |
| 60 | 36987(90%) | 6321(85%) | 5570(75%) | 25021(87%) | 49083(86%) | 74660(89%) | 59345(89%) | 6526(82%) | 3028(82%) | 4478(79%) | 12513(86%) | 18192(89%) |
| 70 | 1863(56%) | 3655(79%) | 5031(80%) | 4052(87%) | 1865(82%) | 3411(90%) | 2123(73%) | 3402(86%) | 2346(82%) | 2791(77%) | 704(49%) | 719(66%) |
| 90 | 840(35%) | 3255(57%) | 8901(62%) | 11125(56%) | 61299(97%) | 135344(98%) | 32767(91%) | 18539(85%) | 4645(64%) | 4076(72%) | 1484(82%) | 608(56%) |
| 100 | 1079(49%) | 1851(59%) | 3423(71%) | 1988(59%) | 2444(82%) | 6027(93%) | 3677(87%) | 8695(92%) | 2813(70%) | 2596(75%) | 565(70%) | 397(66%) |
| 110 | 19896(84%) | 13825(84%) | 4194(73%) | 3669(67%) | 6504(80%) | 11351(92%) | 7407(84%) | 7223(88%) | 4268(84%) | 4983(86%) | 5009(86%) | 5409(81%) |
| 120 | 6568(83%) | 3406(81%) | 3639(77%) | 3602(65%) | 9037(86%) | 12972(93%) | 7122(86%) | 4999(85%) | 3574(51%) | 2379(84%) | 4651(88%) | 4710(87%) |
| 130 | 38258(87%) | 18784(85%) | 19935(85%) | 34627(87%) | 37668(84%) | 34189(86%) | 20881(85%) | 6963(76%) | 20071(85%) | 27134(87%) | 8320(82%) | 15465(84%) |
| 140 | 3941(76%) | 2905(66%) | 6159(78%) | 7692(80%) | 6756(76%) | 8964(85%) | 5139(78%) | 3104(80%) | 13060(26%) | 3562(82%) | 3844(87%) | 4270(87%) |
| 150 | 5760(77%) | 5073(71%) | 8872(77%) | 7268(60%) | 15938(81%) | 19370(87%) | 10467(58%) | 4106(71%) | 12991(24%) | 3532(75%) | 6359(88%) | 8994(92%) |

522 **4.2.3 Cross-verification between MODIS and FY-3D in different regions**

523 The global monitoring area is divided into Africa, America, Asia, Europe, and Oceania. The verification
 524 demonstrates the results with the highest consistence (over 80%) are found in Africa and Asia, and those
 525 in America, Europe, and Oceania show the consistence over 70%. The FY-3D/MERSI- II fire
 526 identification algorithm draws lessons from the MODIS algorithm and has been improved on that basis,
 527 and targeted development has been made for the underlying surface and climatic conditions in China, so
 528 it is necessary to test the matching results in China separately. It shows that China’s regional consistency
 529 of results in China is lower than other continents, only 65%. To further examined the suitability of FY-
 530 3D fire products in China, the accuracy assessment of FY-3D and MODIS fire products was conducted
 531 based on ground truth data and explained in the following sections.

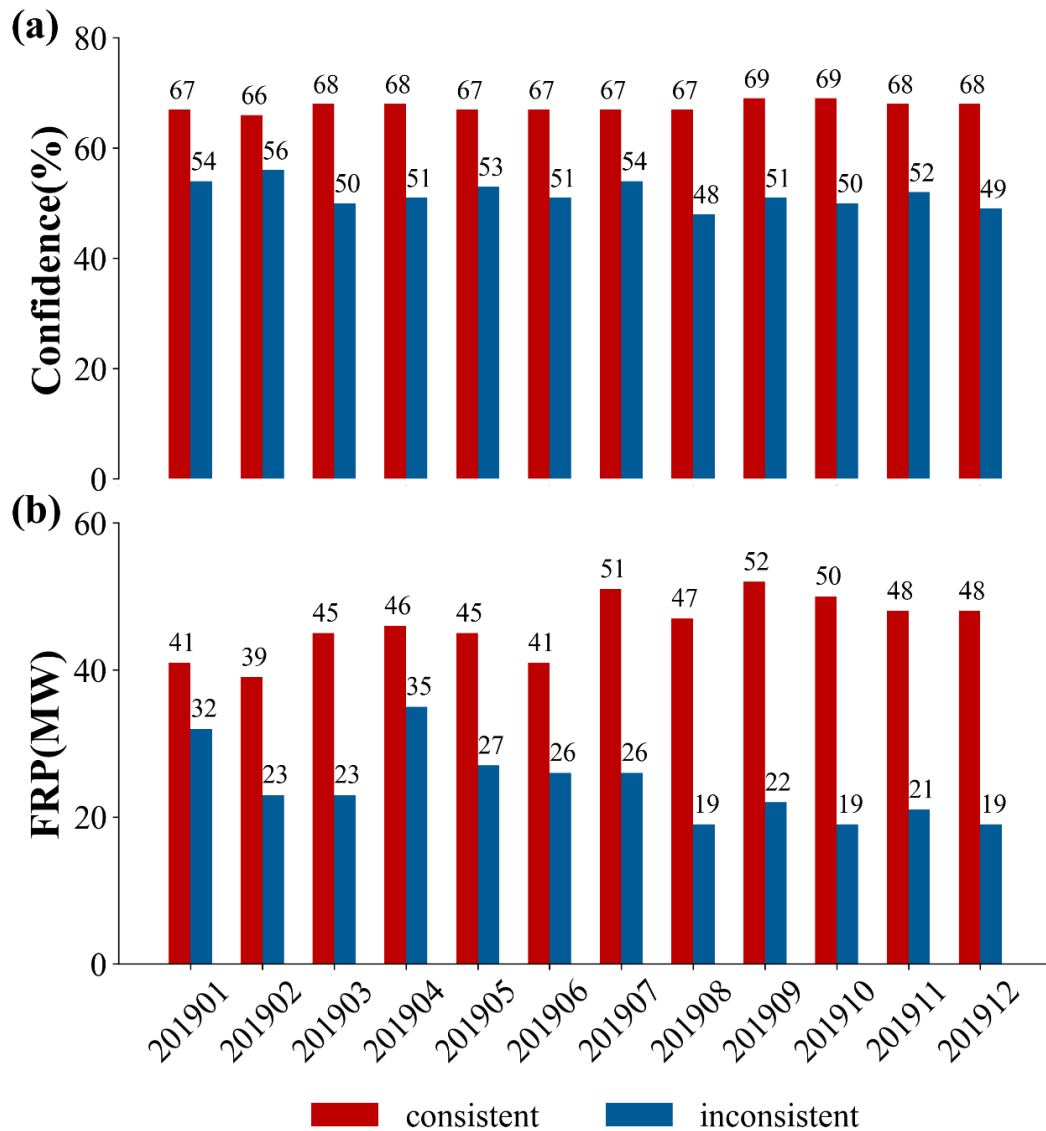


532
 533 Figure 7 Consistence between FY-3D and MODIS fire products under different conditions.
 534 (a)-(c). (a): Consistence between FY-3D and MODIS fire products in different months. (b): Consistence
 535 between FY-3D and MODIS fire products in different regions. (c): Consistence between FY-3D and
 536 MODIS fire products in different underlying surfaces.

537 **4.2.4 Cross-verification of MODIS and FY-3D in terms of fire intensities**

538 The confidence of fire spots and the fire intensity represented by FRP are analyzed respectively, and the
539 data comes from the MODIS fire spot list. Fig. 8(a) and Fig. 8(b) are statistical diagrams of confidence
540 and FRP, respectively. From Fig. 8(a), the confidence of the matched pixels of the two satellites is above
541 66%, while that of the mismatched ones is less than 60% and even lower than 50% in some months. In
542 other words, the higher confidence indicates the higher matching degree. As indicated by Fig. 8(b), the
543 FRP of the matched pixels of two satellites is mostly above 40 MW, while that of the unmatched pixels
544 is less than 40 MW and even lower than 20 MW in some months. Accordingly, the greater fire intensity
545 leads to the greater probability of simultaneous observation by the two satellites and the higher matching
546 degree between their results.

547
548 Two major findings were identified based on the comparison between FY-3D and MODIS fire products
549 in terms of fire intensity: Firstly, the higher the credential of the identified fire, the higher consistence
550 between FY-3D and MODIS fire products. When the credential was larger than 65%, both FY-3D and
551 MODIS could effectively identify the candidate pixel as fire pixel. In other words, the parameter of
552 credential in MODIS fire product provides important reference for fire detection. Secondly, FRP is an
553 index for the heat radiation of the fire. The larger FRP, the larger consistence between FY-3D and MODIS
554 was, indicating a higher accuracy of fire detection. Therefore, the difficulty for fire detection mainly lies
555 in the detection of weak fires.



556

557 **Figure 8** (a)-(b). (a):Confidence of consistent and inconsistent pixels between FY-3D and MODIS fire
 558 products (b): FRP of consistent and inconsistent pixels between FY-3D and MODIS fire products

559

560 **4.3 Accuracy assessment of FY-3D fire products in China based on field collected reference**

561

562 In addition to visual-check and consistence check, we also referred to a large-scale field experiment to
 563 comprehensively assess the suitability of FY-3D fire products in China. STATE GRID Corporation of
 564 China and China Meteorological Administration jointly conducted a fire-detection experiment
 565 throughout 2020 in five provinces Guangdong, Guangxi, Yunnan, Guizhou and Hainan in China. This
 566 experiment was conducted in the following steps. A large number of drones were employed to check the
 567 occurrence of fires. According to the local passing time of FY-3D, these drones reported the coordinate
 568 of actual fires for verifying the accuracy of FY-3D identified fires. The temporal difference between
 569 passing time of FY-3D and reported time was controlled within 1 hour. In this case, both omitted and
 570 misidentified fires could be effectively recognized (As shown in Figure 9). Based on the field collected
 571 reference of fires, we evaluated the suitability of FY-3D fire products in China (Table 8).

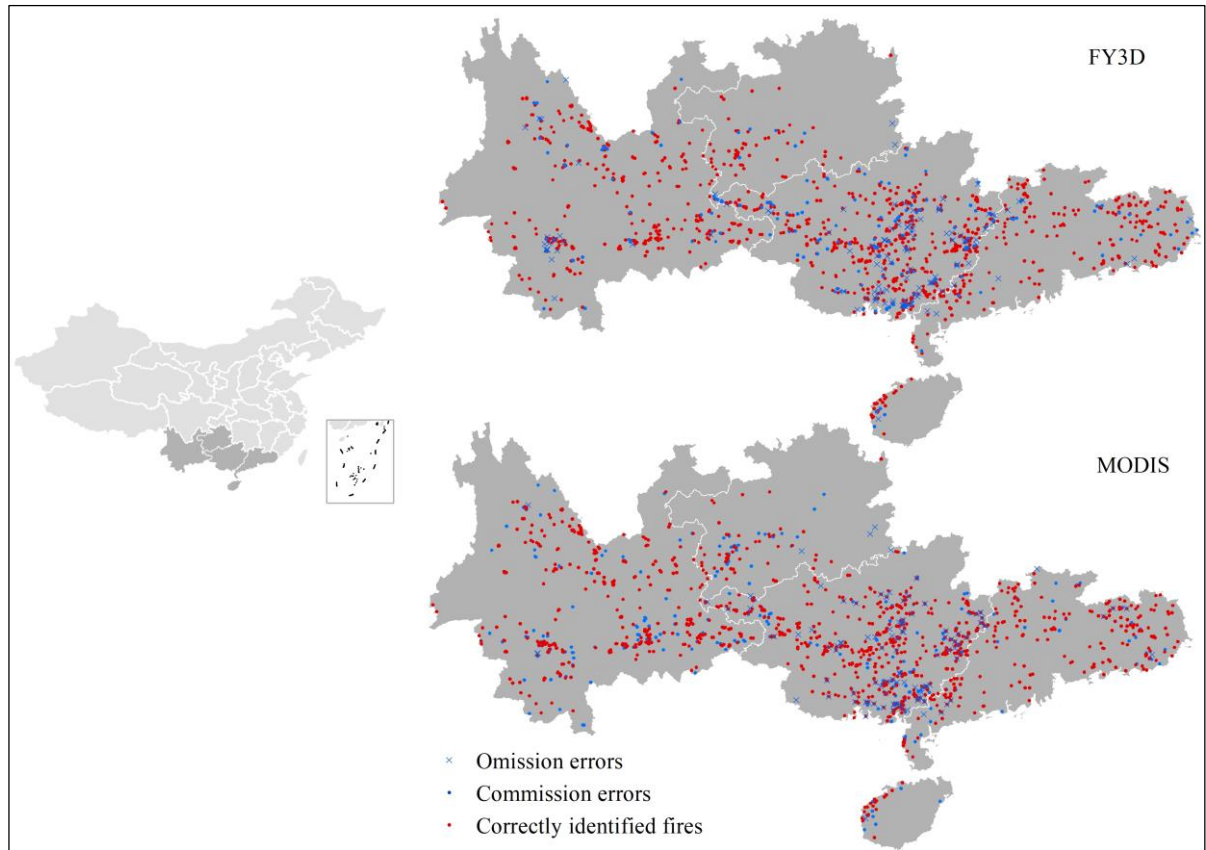


Fig 9 Accuracy assessment of FY-3D fire products in China based ground-based reference

Table 8 Accuracy assessment based on field ground truth

| | Correct Identification | Omission | Commission | Accuracy (%) | Accuracy without omission(%) |
|--------------|------------------------|----------|------------|--------------|------------------------------|
| FY-3D | 1178 | 133 | 172 | 79.43% | 88.50% |
| MODIS | 1201 | 112 | 306 | 74.23% | 79.69% |

As shown in Figure 9 and Table 8, FY-3D products achieved a good accuracy of 79.43% in China. Meanwhile, MODIS also achieved a good accuracy of 74.23%. As introduced above, the omission error of FY-3D and MODIS fire products was mainly attributed to small fire area, which failed to meet the minimum fire area recognizable by sensors. When simply considering the commission error, FY-3D fire products achieved an accuracy of 88.50%, notably higher than that of MODIS (79.69%). This result proved that with the consideration of local underlying surfaces, FY-3D fire products are more suitable for fire monitoring in China.

5 Discussion

5.1 Advantages, limitations and implementations of FY-3D fire products

As satellite instruments keep aging in the harsh space environment, the degradation of sensors is inevitable (Tian et al., 2015). Theoretically, sensor degradation can be corrected through atmospheric

588 calibration. However, during the mission life, the solar diffuser and stability monitor required for
589 atmospheric calibration also change across time (Wang et al., 2012). Since the MODIS instrument has
590 been working for more than 20 years, its performance for fire detection will, if not already, degrade in
591 the future. Furthermore, similar to VIIRS and other algorithms, MODIS fire products may have large
592 uncertainties in such regions as China (Fu et al., 2020; Ying et al., 2019).

593

594 As one major product of the FY-3D meteorological satellite, FY-3D fire products boast the high resolution
595 and accuracy in China by specifically including the underlying surface parameters collected in China.
596 Compared with MODIS and VIIRS, MERSI-II shows the resolution of 250 m in the far-infrared channel,
597 which is the highest among meteorological satellites of the same type. The FY-3D fire identification
598 algorithm learns from the advantages and technical ideas of MODIS and VIIRS fire-identification
599 algorithms. Furthermore, FY-3D fire products have been optimized in terms of auxiliary parameters, fire
600 identification, and re-identification as follows:

601

602 **Auxiliary parameters:** Since the sole use of vegetation index is limited to reflect combustible materials,
603 climatic boundaries and geographical environment data, which have a strong influence on vegetation
604 types and growth, are added to FY-3D fire identification.

605

606 **Fire identification:** FY-3D adopts the adaptive threshold and reduces the limitations caused by fixed
607 thresholds of MODIS and VIIRS algorithms. Meanwhile, FY employs a re-identification index according
608 to geographical latitude, underlying surface types, as well as the influence by cloud, water bodies and
609 bare land, and the comprehensive consideration of multiple influencing factors increases the accuracy of
610 fire identification; Thirdly, since the far-infrared channel plays an important role in fire identification and
611 FY-3D has a high resolution of 250 m in the far-infrared channel, the accuracy of fire identification is
612 improved.

613

614 **Fire re-identification:** FY-3D fire products can be used for both global climate change research and such
615 practical implementations as forest and grassland fire prevention with a higher requirement for accuracy.
616 Based on the initially identified fire spots, FY-3D employed the re-identification index to further remove
617 false fire spots at cloud edges, water body edges, and other high-reflection underlying surfaces.

618

619 MODIS fire product is one of the most significant and frequently employed fire products with mature
620 algorithms. Compared with MODIS, FY-3D receives limited emphasis for its capability of fire
621 monitoring, which is mainly attributed to its short service periods. On one hand, due to its long time
622 series and general reliability, MODIS fire products remained a major choice for monitoring long-term
623 variations of fire spots across the world. However, the long-term running of MODIS sensors led to the
624 growing uncertainties to the quality of recent and future MODIS fire products. In this case, thanks to its
625 similar spatiotemporal resolution, high consistence and less-than-1h difference of visiting time, FY-3D
626 fire products have the potential to be widely employed as the potential alternative and continuity of global
627 MODIS fire products. Meanwhile, FY-3D fire products have a higher reliability in China and its

628 surrounding regions than other fire products. Therefore, FY-3D fire products are an ideal selection for
629 fire monitoring in China.

630

631 The main implementation of FY-3D fire products is fire monitoring. For vast forest and grassland areas,
632 it is inefficient and time-consuming for manual and aircraft patrol to monitor wildfires. Satellite remote
633 sensing can work for continuous space with a wide monitoring range, providing massive information in
634 fire detection, disaster relief, and post-disaster assessment. In addition to the fire spot identification and
635 real-time fire tracking, the impact of pollutants produced by biomass combustion on the environment is
636 another important topic. In China and Southeast Asia, air pollution caused by biomass burning has been
637 intensified in recent years. Agricultural activities such as crop-residue burning and wildfires (e.g. forest
638 fires and grassland fires) emit airborne pollutants (e.g. PM_{2.5}, PM₁₀, CO). In this regard, FY-3D fire
639 products can be used as the emission sources for estimating its environmental effects.

640 **5.2 Future extension of FY-3D fire products**

641 China has just launched FY-3E and FY-4B satellites in June and July, 2021. Amid the launch and
642 operation of a new generation of Fengyun meteorological satellites, the accuracy and timeliness of fire
643 monitoring by meteorological satellites have been largely enhanced. Thanks to the improved
644 meteorological data, which provides useful reference to understand the current status of combustibles
645 and potential fire risk, FY-3D satellite will be taken as a better data source to produce various secondary
646 products for fire monitoring and prediction. Based on traditional fire spot identification, further research
647 should concentrate on the assessment of fire area, estimation of biomass carbon emission, prediction of
648 smoke impact, and early warning of forest and grassland fire using the series of Fengyun meteorological
649 satellites. For instance, the water content of combustibles is closely related to temperature, light, and
650 cloud cover, which is an important indicator in forest and grassland fire forecasts. However, this variable
651 was rarely considered in previous fire products. Based on a series of products from Fengyun
652 meteorological satellites, such as surface temperature, vegetation index, surface evapotranspiration, solar
653 radiance, and cloud cover, FY-3D fire products can be improved by establishing an estimation model for
654 the water content of combustibles. Meanwhile, with the fire products such as fire spot and smoke, and
655 the meteorological products such as wind field data from Fengyun series satellites, we can predict the
656 impact of smoke caused by forest and grassland fires on the atmospheric environment in the surrounding
657 areas. In the future implementations, Fengyun meteorological satellites will play a greater role in
658 monitoring, early warning, and forecasting global fires and their ecological impacts.

659

660 **6 Data availability**

661 The MYD14A1 Version 6 is available via the NASA FIRMS portal
662 (<https://firms.modaps.eosdis.nasa.gov/map/>, NASA FIRMS, 2021). FY-3D fire products are now
663 downloadable from our official website (<http://satellite.nsmc.org.cn/portalsite/default.aspx>, NSMC, 2021)
664 using registered account and password. For the convenience of data check and trial experiments, a test
665 account is provided as
666 Account: 1256931756@qq.com
667 Password: yangjing1211

668 **7 Conclusions**

669 With a similar spatial and temporal resolution, we produced FY-3D global fire products, aiming to serve
670 as the potential alternative and continuity for MODIS fire products. The sensor parameters and major
671 algorithms for noise detection and fire identification in FY-3D products were introduced. For visual-
672 check-based accuracy assessment, five typical regions, Africa, South America, Indo-China Peninsula,
673 Siberia and Australia, across the globe were selected and the overall accuracy exceeded 94%. We also
674 compared the FY-3D and MODIS fire products for their consistence. The result suggested that the overall
675 consistence was 84.4%, with a fluctuation across seasons, surface types and regions. The high accuracy
676 and consistence with MODIS products proved that FY-3D fire product was an ideal tool for global fire
677 monitoring. Based on field-collected reference data, we further evaluated the suitability of FY-3D fire
678 products in China. The overall accuracy and accuracy (without considering omission errors) was 79.43%
679 and 88.50% respectively, higher than that of MODIS fire products. Since detailed geographical
680 conditions in China were considered, FY-3D products should be preferably employed for monitoring
681 fires and estimating its environment effects in China.

682 **Author contributions**

683 J, C., W.Z and C,L produced FY-3D global fire products and the official website. J.C., Z.C., B, G., M, L.
684 conceived the manuscript. J,C., C,Z., Q, Y., M.X., X,C., and J, Y. conducted data analysis and produced
685 Figures. J.C and Z.C wrote the draft. Z.C and M,L. reviewed and revised the manuscript.

686 **Competing interests**

687 The authors have no competing interests.

688 **Financial support**

689 This work was supported by the National Natural Science Foundation of China (Grant No.42171399)
690 and National Key R&D Program of China (2021YFC3000300).

691 **References**

- 692 Abram, N.J., Henley, B.J. and Sen Gupta, A.: Connections of climate change and variability to large and
693 extreme forest fires in southeast Australia, *Commun. Earth Environ.*, 2, 8,
694 <https://doi.org/10.1038/s43247-020-00065-8>, 2021.
- 695 Alisjahbana, A.S. and Busch, J.M.: Forestry, Forest Fires, and Climate Change in Indonesia. *Bull. of*
696 *Indones. Econ. Stud.*, 53, 111–136, <https://doi.org/10.1080/00074918.2017.1365404>, 2017.
- 697 Andela, N., Morton, D.C., Giglio, L., Paugam, R., Chen, Y., Hantson, S., van der Werf, G. R., and
698 Randerson, J.T.: The Global Fire Atlas of individual fire size, duration, speed and direction, *Earth Syst.*
699 *Sci. Data*, 11, 529–552, <https://doi.org/10.5194/essd-11-529-2019>, 2019.
- 700 Barnes, B.B., Cannizzaro, J.P., English, D.C., and Hu, C.: Validation of VIIRS and MODIS reflectance
701 data in coastal and oceanic waters: An assessment of methods, *Remote Sens. Environ.*, 220, 110-123,
702 <https://doi.org/10.1016/j.rse.2018.10.034>, 2019.
- 703 Boles, S.H. and Verbyla, D.L.: Comparison of three AVHRR-based fire detection algorithms for interior
704 Alaska, *Remote Sens. Environ.*, 72, 1-16, [https://doi.org/10.1016/S0034-4257\(99\)00079-6](https://doi.org/10.1016/S0034-4257(99)00079-6), 2000.
- 705 Cerda, Lloret, F., Ruiz, J.E., and Vandermeer, J.H.: Tree mortality following ENSO-associated fires and
706 drought in lowland rain forests of Eastern Nicaragua, *For. Ecol. Manage.*, 265, 248-257,
707 <https://doi.org/10.1016/j.foreco.2011.10.034>, 2012.
- 708 Cochrane, M.: Fire science for rainforests, *Nature*, 421, 913-919, <https://doi.org/10.1038/nature01437>,
709 2003.
- 710 Doelling, D.R., Wu, A., Xiong, X., Scarino, B.R., Bhatt, R., Haney, C.O., Morstad, D., and Gopalan, A.:
711 The radiometric stability and scaling of collection 6 Terra-and Aqua-MODIS VIS, NIR, and SWIR
712 spectral bands, *IEEE Trans. Geosci. Remote Sensing*, 53, 4520-4535,
713 <https://doi.org/10.1109/TGRS.2015.2400928>, 2015.
- 714 Dozier, J.: A method for satellite identification of surface temperature fields of subpixel resolution,
715 *Remote Sens. Environ.*, 74, 33-38, [https://doi.org/10.1016/0034-4257\(81\)90021-3](https://doi.org/10.1016/0034-4257(81)90021-3), 1981.
- 716 Fang, H., Wei, S., and Liang, S.: Validation of MODIS and CYCLOPES LAI products using global field
717 measurement data, *Remote Sens. Environ.*, 119, 43-54, <https://doi.org/10.1016/j.rse.2011.12.006>, 2012.
- 718 Fensholt, R., and Proud, S.R.: Evaluation of earth observation based global long term vegetation trends—
719 Comparing GIMMS and MODIS global NDVI time series, *Remote Sens. Environ.*, 119, 131-147,
720 <https://doi.org/10.1016/j.rse.2011.12.015>, 2012.
- 721 Flannigan, M.D. and Haar, T.H.: Forest fire monitoring using NOAA satellite AVHRR, *Can. J. For. Res.*,
722 16, 975-982, <https://doi.org/10.1139/x86-171>, 1986.
- 723 Giglio, L., Boschetti, L., Roy, D.P., Humber, M.L., and Justice, C.O.: The Collection 6 MODIS burned
724 area mapping algorithm and product, *Remote Sens. Environ.*, 217, 72-85,
725 <https://doi.org/10.1016/j.rse.2018.08.005>, 2018.

726 Guo, J., Zhang, X., Cao, C., Che, H., Liu, H., Gupta, P., Zhang, H., Xu, M., and Li, X.: Monitoring haze
727 episodes over the Yellow Sea by combining multisensor measurements, *Int. J. Remote Sens.*, 31, 4743-
728 4755, <https://doi.org/10.1080/01431161.2010.485213>, 2010.

729 Guo, L., Ma, Y., Tigabu, M., Guo, X., Zheng, W., and Guo, F.: Emission of atmospheric pollutants during
730 forest fire in boreal region of China, *Environ. Pollut.*, 264, 114709,
731 <https://doi.org/10.1016/j.envpol.2020.114709>, 2020.

732 Hall, J.V., Zhang, R., Schroeder, W., Huang, C., and Giglio, L.: Validation of GOES-16 ABI and MSG
733 SEVIRI active fire products, *Int. J. Appl. Earth Obs. Geoinf.*, 83, 101928,
734 <https://doi.org/10.1016/j.jag.2019.101928>, 2019.

735 Huff, A.K., Kondragunta, S., Zhang, H., and Hoff, R.M.: Monitoring the impacts of wildfires on forest
736 ecosystems and public health in the exo-urban environment using high-resolution satellite aerosol
737 products from the visible infrared imaging radio-meter suite (VIIRS), *Environ. Health Insights*, 9s2,
738 EHI.S19590, <https://doi.org/10.4137/ehi.s19590>, 2015.

739 Jacobson, M.Z.: Effects of biomass burning on climate, accounting for heat and moisture fluxes, black
740 and brown carbon, and cloud absorption effects, *J. Geophys. Res. Atmos.*, 119, 2014JD021861,
741 <https://doi.org/10.1002/2014JD021861>, 2014.

742 Jethva, H., Torres, O., and Field, R.D.: Connecting Crop Productivity, Residue Fires, and Air Quality
743 over Northern India, *Sci. Rep.*, 9, 16594, <https://doi.org/10.1038/s41598-019-52799-x>, 2019.

744 Johnston, F.H., Henderson, S.B., Chen, Y., Randerson, J.T., Marlier, M., DeFries, R.S., Kinney, P.,
745 Bowman, D.M., and Brauer, M.: Estimated global mortality attributable to smoke from landscape fires,
746 *Environ. Health Perspect*, 120, <https://doi.org/10.1289/ehp.1104422>, 2012.

747 Kaufman, Y.J., Kleidman, R.G., and King, M.D.: SCAR - B fires in the tropics: properties and remote
748 sensing from EOS-MODIS, *J. Geophys. Res.-Atmos.*, 103(D24): 31955-31968,
749 <https://doi.org/10.1029/98JD02460>, 1998.

750 Kaufman, Y.J., Setzer, A., and Justice, C.: Remote Sensing of Biomass Burning in the Tropics, *Fire in*
751 *the Tropical Biota*, 84, 371-399, https://doi.org/10.1007/978-3-642-75395-4_16, 1990.

752 Keegan, K.M., Albert, M.R., McConnell, J.R., and Baker, I.: Climate change and forest fires
753 synergistically drive widespread melt events of the Greenland Ice Sheet, *Proc. Natl. Acad. Sci. U.S.A.*,
754 111, 7964–7967, <https://doi.org/10.1073/pnas.1405397111>, 2014.

755 Keeley, J.E., Bond, W.J., Bradstock, R.A., Pausas, J.G., and Rundel, P.W.: *Fire in Mediterranean*
756 *ecosystems: Ecology, evolution and management*, Cambridge University Press, Cambridge, United
757 Kingdom, 2011.

758 Kelly, L.T., Giljohann, K.M., Duane, A., Aquilué N., Archibald, S., and Batllori, E.: Fire and biodiversity
759 in the Anthropocene, *Science*, 370, eabb0355, <https://doi.org/10.1126/science.abb0355>, 2020.

760 Li, F., Zhang, X., Kondragunta, S., and Lu, X.: An evaluation of advanced baseline imager fire radiative
761 power based wildfire emissions using carbon monoxide observed by the Tropospheric Monitoring

762 Instrument across the conterminous United States, *Environ. Res. Lett.*, 15, 094049,
763 <https://doi.org/10.1088/1748-9326/ab9d3a>, 2020.

764 Li, J., Bo, Y., and Xie, S.: Estimating emissions from crop residue open burning in China based on
765 statistics and MODIS fire products, *J. Environ. Sci.*, 44, 158-170,
766 <https://doi.org/10.1016/j.jes.2015.08.024>, 2016.

767 Lin, Z., Chen, F., Li, B., Yu, B., Shirazi, Z., Wu, Q., and Wu, W.: FengYun-3C VIRR Active Fire
768 Monitoring: Algorithm Description and Initial Assessment Using MODIS and Landsat Data, *IEEE Trans.*
769 *Geosci. Remote Sens.*, 55, 6420-6430, <https://doi.org/10.1109/TGRS.2017.2728103>, 2017.

770 Liu, T., Marlier, M.E., DeFries, R.S., Westervelt, D.M., Xia, K.R., Fiore, A.M., Mickley, L.J., Cusworth,
771 D.H., and Milly, G.: Seasonal impact of regional outdoor biomass burning on air pollution in three Indian
772 cities: Delhi, Bengaluru, and Pune, *Atmos. Environ.*, 172, 83–92,
773 <https://doi.org/10.1016/j.atmosenv.2017.10.024>, 2018.

774 Liu, Y., Hill, M.J., Zhang, X., Wang, Z., Richardson, A.D., Hufkens, K., Filippa, G., Baldocchi, D.D.,
775 Ma, S., and Verfaillie, J.: Using data from Landsat, MODIS, VIIRS and PhenoCams to monitor the
776 phenology of California oak/grass savanna and open grassland across spatial scales, *Agric. For. Meteorol.*,
777 237, 311-325, <https://doi.org/10.1016/j.agrformet.2017.02.026>, 2017.

778 Lyapustin, A., Wang, Y., Xiong, X., Meister, G., Platnick, S., Levy, R., Franz, B., Korkin, S., Hilker, T.,
779 and Tucker, J.: Scientific impact of MODIS C5 calibration degradation and C6+ improvements, *Atmos.*
780 *Meas. Tech.*, 7, 4353-4365, <https://doi.org/10.5194/amt-7-4353-2014>, 2014.

781 Marlier, M.E., DeFries, R.S., Kim, P.S., Koplitz, S.N., Jacob, D.J., Mickley, L.J., and Myers, S.S.: Fire
782 emissions and regional air quality impacts from fires in oil palm, timber, and logging concessions in
783 Indonesia, *Environ. Res. Lett.*, 10, 085005, <https://doi.org/10.1088/1748-9326/10/8/085005>, 2015.

784 Matson, M. and Schneider, S.R.: Fire Detection Using the NOAA-Series Satellite, NOAA Technical
785 Report NESDIS, 7, 1984.

786 Mohajane, M., Costache, R., Karimi, F., Pham, Q.B., Essahlaoui, A., Nguyen, H., Laneve, G., and Oudija,
787 F.: Application of remote sensing and machine learning algorithms for forest fire mapping in a
788 Mediterranean area, *Ecol. Indic.*, 129, 107869, <https://doi.org/10.1016/j.ecolind.2021.107869>, 2021.

789 Moritz, M.A., Parisien, M.A., Batllori, E., Krawchuk, M.A., Van Dorn, J., Ganz, D.J., and Hayhoe, K.:
790 Climate change and disruptions to global fire activity, *Ecosphere*, 3, 1–22, <https://doi.org/10.1890/ES11-00345.1>, 2012.

792 NASA FIRMS: MODIS fire products MYD14A1 V6.1 2019 [data set], available at:
793 <https://firms.modaps.eosdis.nasa.gov/map/>, last access 10 January 2021.

794 NSMC: FY-3D fire products 2018-2019 [data set], available at:
795 <http://satellite.nsmc.org.cn/portalsite/default.aspx>, last access 10 January 2021.

796 Oliveira, M., Delerue-Matos, C., Pereira, M.C., and Morais, S.: Environmental Particulate Matter Levels
797 during 2017 Large Forest Fires and Megafires in the Center Region of Portugal: A Public Health Concern?
798 *Int. J. Environ. Res. Public Health*, 17, 1032, <https://doi.org/10.3390/ijerph17031032>, 2020.

799 Sayer, A., Hsu, N., Bettenhausen, C., Jeong, M.J., and Meister, G.: Effect of MODIS Terra radiometric
800 calibration improvements on Collection 6 Deep Blue aerosol products: Validation and Terra/Aqua
801 consistency, *J. Geophys. Res.-Atmos.*, 120, 12,157-112,174, <https://doi.org/10.1002/2015JD023878>,
802 2015.

803 Schroeder, W., Oliva, P., and Giglio, L.: The New VIIRS 375 m active fire detection data product:
804 Algorithm description and initial assessment, *Remote Sens. Environ.*, 143, 85-96,
805 <https://doi.org/10.1016/j.rse.2013.12.008>, 2014.

806 Sharma, A., Wang, J., and Lennartson, E.M.: Intercomparison of MODIS and VIIRS Fire Products in
807 Khanty-Mansiysk Russia: Implications for Characterizing Gas Flaring from Space, *Atmosphere*, 8, 95,
808 <https://doi.org/10.3390/atmos8060095>, 2017.

809 Stephenson, C., Handmer, J., and Betts, R.: Estimating the economic, social and environmental impacts
810 of wildfires in Australia, *Environ. Hazards*, 12, 93–111, <https://doi.org/10.1080/17477891.2012.703490>,
811 2013.

812 Tian, F., Fensholt, R., Verbesselt, J., Grogan, K., Horion, S., and Wang, Y.: Evaluating temporal
813 consistency of long-term global NDVI datasets for trend analysis, *Remote Sens. Environ.*, 163, 326-340,
814 <https://doi.org/10.1016/j.rse.2015.03.031>, 2015.

815 Twohy, C.H., Toohey, D.W., Levin, E.J., DeMott, P.J., Rainwater, B., Garofalo, L.A., Pothier, M.A.,
816 Farmer, D.K., Kreidenweis, S.M., and Pokhrel, R.P.: Biomass Burning Smoke and Its Influence on
817 Clouds Over the Western US, *Geophys. Res. Lett.*, 48, e2021GL094224,
818 <https://doi.org/10.1029/2021GL094224>, 2021.

819 Volkova, L., Roxburgh, S.H., Surawski, N.C., Meyer, C.P., and Weston, C.J.: Improving reporting of
820 national greenhouse gas emissions from forest fires for emission reduction benefits: An example from
821 Australia, *Environ. Sci. Policy*, 94, 49-62, <https://doi.org/10.1016/j.envsci.2018.12.023>, 2019.

822 Wang, D., Guo, J., Chen, A., Bian, L., Ding, M., Liu, L., Lv, Y., Li, J., Guo, X., and Han, Y.: Temperature
823 inversion and clouds over the Arctic Ocean observed by the 5th Chinese National Arctic Research
824 Expedition, *J. Geophys. Res.-Atmos.*, 125, e2019JD032136, <https://doi.org/10.1029/2019JD032136>,
825 2020.

826 Wang, D., Morton, D., Masek, J., Wu, A., Nagol, J., Xiong, X., Levy, R., Vermote, E., and Wolfe, R.:
827 Impact of sensor degradation on the MODIS NDVI time series, *Remote Sens. Environ.*, 119, 55-61,
828 <https://doi.org/10.1016/j.rse.2011.12.001>, 2012.

829 Wickramasinghe, C., Wallace, L., Reinke, K., and Jones, S.: Intercomparison of Himawari-8 AHI-FSA
830 with MODIS and VIIRS active fire products, *Int. J. Digit. Earth*, 13, 457-473,
831 <https://doi.org/10.1080/17538947.2018.1527402>, 2018.

832 Wintle, B.A., Legge, S., and Woinarski, J.: After the Megafires: What Next for Australian Wildlife?
833 Trends Ecol. Evol., 35, 753-757, <https://doi.org/10.1016/j.tree.2020.06.009>, 2020.

834 Xie, Y., Zhang, Y., Xiong, X., Qu, J.J., and Che, H.: Validation of MODIS aerosol optical depth product
835 over China using CARSNET measurements, Atmos. Environ., 45, 5970-5978,
836 <https://doi.org/10.1016/j.atmosenv.2011.08.002>, 2011.

837 Xiong, X., Angal, A., Twedt, K.A., Chen, H., Link, D., Geng, X., Aldoretta, E., and Mu, Q.:MODIS
838 reflective solar bands on-orbit calibration and performance, IEEE Trans. Geosci. Remote Sensing, 57,
839 6355-6371, <http://doi.org/10.1109/TGRS.2019.2905792>, 2019.

840 Xu, W., Wooster, M.J., Kaneko, T., He, J., Zhang, T., and Fisher, D.: Major advances in geostationary
841 fire radiative power (FRP) retrieval over Asia and Australia stemming from use of Himarawi-8 AHI,
842 Remote Sens. Environ., 193, 138-149, <https://doi.org/10.1016/j.rse.2017.02.024>, 2017.

843 Yuchi, W., Yao, J., Kathleen, E.M., Roland, S., Radenko, P., Didier, D., Michael, D.M., and Sarah, B.H.:
844 Blending forest fire smoke forecasts with observed data can improve their utility for public health
845 applications, Atmos. Environ., 145, 308-317, <https://doi.org/10.1016/j.atmosenv.2016.09.049>, 2016.

846 Zhang, Z., Feng, Z., Zhang, H., Zhao, J., Yu, S., and Du, W.: Spatial distribution of grassland fires at the
847 regional scale based on the MODIS active fire products. Int. J. Wildland Fire, 26, 209-218,
848 <https://doi.org/10.1071/WF16026>, 2017.

849